Utrecht University

Department of Physics

Bachelor Thesis

Sacha de Wind

Constructing the excess Helmholtz free-energy functional of a supercritical Lennard-Jones fluid with Machine Learning

Supervisors:

Prof. dr. R. van Roij
Institute for Theoretical Physics

Prof. dr. ir. M. Dijkstra
Debye Institute for Nanomaterials Science

10 June 2019

Abstract

Classical Density Functional Theory is an active topic within Soft Condensed Matter Theory and is mainly concerned with constructing density functionals that describe the properties of classical many-body systems such as gases and fluids. These functionals of the particle density distribution are unique for a given particle interaction potential, but there is no straightforward way to find or approximate them except for very simple systems like the ideal gas or hard spheres. In this thesis we use Machine Learning to approximate the excess Helmholtz free-energy functional $\mathcal{F}_{exc}^{LJ}[\rho(\mathbf{r})]$ of a supercritical Lennard-Jones fluid in planar geometries in $3D$. Monte Carlo simulations are used to generate a set of density profiles that serves as a training data set from which an Ansatz for $\mathcal{F}_{exc}^{LJ}[\rho(\mathbf{r})]$ learns. Overall the trained functional outperforms Mean Field Theory at predicting density profiles and the equation of state, although predictive power is limited at low temperatures and for chemical potentials slightly above the ideal-gas regime. The trained functional does not exactly scale linearly with the temperature, in contrast to our expectations, and performs significantly better at high than at low temperatures. We discuss the limitations of our method and implications for future research concerning the use of Machine Learning for classical DFT.

Contents

1 Introduction

Density functional theory (DFT) is a powerful tool that originated in the 1960s in the context of the quantum theory of electrons in atoms, molecules and solids[1]. Walter Kohn and Pierre Hohenberg showed that the ground state properties of a quantum-mechanical many-body system are uniquely determined by its electron density distribution. They defined an energy functional of this density and proved that this functional achieves its minimum value only at the equilibrium electron density profile of the system. Thus, the density of the ground state and hence the properties of the system in an arbitrary external potential can be found by minimizing the energy functional, which generally has to be done numerically. Because of the relatively high computational efficiency of this method compared to older methods based on many-body wavefunctions[2], density functional theory had a substantial impact on solid state physics and quantum chemistry and became one of the most popular calculational methods.

Not many years later density functional theory was reformulated in terms of classical statistical mechanics, and the new theory inherited the name classical density functional theory. It was shown that for a specific particle interaction potential, the intrinsic Helmholtz free-energy functional $\mathcal{F}[\rho(\mathbf{r})]$ of a classical many-body system is a unique functional of the density of the system and is independent of the external potential $V_{ext}(\mathbf{r})$ and chemical potential μ. Given $\mathcal{F}[\rho(\mathbf{r})]$, a self-consistency equation for the equilibrium density $\rho_0(\mathbf{r})$ can be derived. So when $\mathcal{F}[\rho(\mathbf{r})]$ is known, it is possible to compute the equilibrium density given some $V_{ext}(\mathbf{r})$ and μ. Similar to the quantum-mechanical case, where the exact form of the energy functional is unknown, $\mathcal{F}[\rho(\mathbf{r})]$ is not exactly known either for nonzero particle interaction potentials. An exception is the ideal gas for which the functional is exactly known, and this makes it possible to split the free-energy functional for an arbitrary type of interaction potential into an ideal-gas intrinsic free-energy contribution $\mathcal{F}^{id}[\rho(\mathbf{r})]$, and a so-called excess intrinsic free-energy contribution $\mathcal{F}^{exc}[\rho(\mathbf{r})]$ due to the particle-particle interactions.

Over the past 50 years, considerable theoretical and computational effort has gone into approximating $\mathcal{F}^{exc}[\rho(\mathbf{r})]$ for different types of interaction potentials. In 1989 Yasha Rosenfeld developed the so-called Fundamental Measure Theory for hard-sphere mixtures, which is based on the underlying geometrical properties of hard spheres. This density functional theory yielded excellent equilibrium density predictions for different physical situations, including adsorbtion of hard spheres at a hard wall, compared to Monte Carlo simulations. It was later improved by Rosenfeld and Tarazona to account for more extreme situations such as freezing transitions[3].

The Lennard-Jones potential is a mathematically simple potential that approximates the interaction of most neutral pairs of atoms or small molecules. Because it is so widely applicable this potential is often studied, not unlike hard spheres. The interaction is strongly repulsive at short distances and weakly attractive at medium to long distances. For the Lennard-Jones interaction potential, the exact excess free-energy functional is unknown despite significant theoretical research. A mathematically simple mean field approximation is known which yields reasonably accurate predictions compared to Monte Carlo simulations, but overall the

results are not satisfactory. Using the Benedict-Webb-Rubin equation of state, a weighted density functional was constructed which performs significantly better and yields good results in most situations such as predicting the density in slit-like pores[4]. Similar improvement was achieved by a mathematically refined perturbative approach[5]. However, the physical interpretation of the above methods remains difficult due to requiring many experimentally determined constants and very high order correlation functions, respectively. To assist in approximating functionals in physics and to eventually gain deeper theoretical insight, Machine Learning methods were recently introduced in the context of functional building[7][8].

Machine Learning (ML) methods are extremely widely used for countless tasks including pattern recognition, image classification, interaction in video games and news and social media filtering[6]. Usually a very general model is postulated in which some mathematical objects such as parameters or weighting kernels are to be estimated by giving the model sample data, a process which is called 'training'[6]. ML can therefore be seen as a subset of statistics and / or of artificial intelligence. The model that is built by using ML techniques can then be used to make predictions and decisions in situations like those for which the model was trained. Usually the most difficult aspect of using ML techniques for scientific purposes is not the implementation of the training process, but the generation of high quality data and the interpretation of the results. Because of the tremendous succes of using ML in many fields it has recently been introduced in physics as well, initially for constructing the kinetic energy functional in $1D$ in the context of quantum-mechanical DFT[7]. This was successful, however in the 3-dimensional case it was not possible to approximate the functional explicitly and ML was used to determine the map between the external potential and the electron density. The latter yielded very accurate predictions but lacks implications for theoretical insight.

In late 2018 ML was used for the first time to construct a classical density functional, namely the excess Helmholtz free-energy functional of a $1D$ Lennard-Jones fluid[8]. Data was generated by Monte Carlo (MC) simulations. Different Ansatzes for the form of the functional, all of them in terms casted as products of convolutions of the density with weighting kernels, were tried. Good results were achieved, except for the equation of state at low temperatures.

In this thesis we apply ML to approximate the excess Helmholtz free-energy functional $\mathcal{F}^{exc}[\rho(\mathbf{r})]$ of a $3D$ Lennard-Jones fluid in planar geometries. For the first time, we compare the predictions of different Ansatzes for the functional to those of MF and MC and discuss the physical interpretation of the results. We briefly review the theoretical background of classical density functional theory. Next we describe the method and settings of the Monte Carlo simulations used for data generation, and explain the implementation of the training process. Subsequently we discuss the results and conclude with the key findings.

2 Theoretical background of Classical Density Functional Theory

In this chapter we briefly review classical density functional theory. We shall assume that the reader is familiar with basic statistical mechanics and the grand canonical ensemble. In depth knowledge of the Calculus of Variations is not necessary.

2.1 Some essential definitions and notations

Here we closely follow the notational conventions of [9]. In statistical mechanics, the grand canonical ensemble (also known as the μVT ensemble) considers a system with a fixed chemical potential μ, volume V and temperature T in thermodynamic equilibrium with a large reservoir of particles. We shall consider only the case of N spherically symmetric, identical particles with positions $\mathbf{r}^N = (\mathbf{r}_1 \cdots \mathbf{r}_N)$ and linear momenta $\mathbf{p}^N = (\mathbf{p}_1 \cdots \mathbf{p}_N)$. The Hamiltonian of N particles is given by $H_N = K + \Phi + \mathcal{V}$, respectively the sum of the total kinetic energy K, the energy due to particle-particle interactions Φ and the energy due to an external field $\mathcal{V}$. Thus,

$$\begin{aligned} K &= \sum_{i=1}^{N} \frac{\mathbf{p}^2{}_i}{2m}; \\ \Phi &= \Phi\left(\mathbf{r}_1 \cdots \mathbf{r}_N\right); \\ \mathcal{V} &= \sum_{i=1}^{N} V_{ext}\left(\mathbf{r}_i\right). \end{aligned} \tag{2.1}$$

In equilibrium, the probability density of the system to be in a microstate of N particles at point $(\mathbf{r}^N, \mathbf{p}^N)$ in the phase space is given by

$$f_0(\mathbf{r}^N, \mathbf{p}^N, N) = \frac{1}{\Xi} \exp\left[\beta(\mu N - H_N)\right], \tag{2.2}$$

where the normalization factor is the grand canonical partition function:

$$\Xi \;=\; \sum_{N=0}^{\infty} \frac{1}{N! h^{3N}} \int d\mathbf{p}_1 \cdots d\mathbf{p}_N d\mathbf{r}_1 \cdots d\mathbf{r}_N \exp\left[\beta(\mu N - H_N)\right]. \tag{2.3}$$

Here $\beta = \frac{1}{k_b T}$ is the inverse temperature, with k_b Boltzmann's constant, h is Planck's constant so as to make the result dimensionless and the familiar $\frac{1}{N!}$ factor accounts for overcounting due to identical particles.
In analogy with standard probability theory, the expectation of any function (say: a thermodynamic operator) $\widehat{O} = \widehat{O}(\mathbf{r}^N, \mathbf{p}^N, N)$ is

$$\mathrm{Tr}_{cl} f_0 \widehat{O} \equiv \langle \widehat{O} \rangle, \tag{2.4}$$

where we define the so-called classical trace:

$$\mathrm{Tr}_{cl} \equiv \sum_{N=0}^{\infty} \frac{1}{N!h^{3N}} \int d\mathbf{p}_1 \cdots d\mathbf{p}_N d\mathbf{r}_1 \cdots d\mathbf{r}_N, \tag{2.5}$$

for which $\mathrm{Tr}_{cl} f_0 = 1$ by construction.

An important thermodynamic operator is the density operator $\widehat{\rho}(\mathbf{r}) = \sum_{i=1}^{N} \delta(\mathbf{r} - \mathbf{r}_i)$, of which the expectation is the equilibrium density distribution of the system:

$$\mathrm{Tr}_{cl} f_0 \widehat{\rho}(\mathbf{r}) = \langle \widehat{\rho}(\mathbf{r}) \rangle \equiv \rho_0(\mathbf{r}). \tag{2.6}$$

The grand canonical partition function Ξ contains all the thermodynamic information of the system in thermal equilibrium, and full knowledge of it would provide the ability to calculate the expectation of any thermodynamic observable $\widehat{O}$ of interest, by Eq.(2.4). However, calculating Ξ exactly by integration is clearly impossible for almost all situations involving even slightly complex or weak interaction potentials, due to the integrand which couples the integration variables. Numerically it is also impossible, because of the high dimension of the phase space. An argument for this based on an equivalent one in [10] goes as follows. In D spatial dimensions with N particles the phase space has dimension (roughly, due to conservation laws) equal to $2ND$. Suppose we take $D = 3$, $N = 1000$, and a conservative 10 grids points per integration variable. The total number of grid points of the entire phase space is then 10^{6000} and on this grid the integral is not computable by any craft that we on earth possess.

2.2 The grand potential and the intrinsic Helmholtz free energy

The grand potential, the thermodynamic potential of the grand canonical ensemble, is given by:

$$\Omega = -k_B T \ln \Xi. \tag{2.7}$$

It is a *functional* of $f_0 = f_0(\mathbf{r}^N, \mathbf{p}^N, N)$ and hence of $V_{ext}(\mathbf{r})$, through Ξ.
Now consider the following functional of some normalized non-negative probability density f:

$$\Omega[f] = \mathrm{Tr}_{cl}\{f \cdot (H_N - \mu N + \beta^{-1} \ln f)\}. \tag{2.8}$$

Here $\Omega[f]$ and f are arbitrary and supposedly unrelated to the grand potential Ω and f_0.

We will show that the functional of Eq. (2.8) possesses two properties of great interest. First, evaluated at the equilibrium probability density f_0 it reduces to the grand potential Ω:

$$\begin{aligned} \Omega[f_0] &= \mathrm{Tr}_{cl}\{f_0 \cdot (H_N - \mu N + \beta^{-1} \ln f_0)\} \\ &= \mathrm{Tr}_{cl}\{f_0 \cdot (-k_B T \ln \Xi)\} \\ &= -k_B T \ln \Xi \\ &= \Omega, \end{aligned} \tag{2.9}$$

where the second equality follows from rewriting Eq.(2.2) and the third follows from the fact that Ξ is independent of $\mathbf{r}^N$ and $\mathbf{p}^N$ and that f_0 is normalized.

Second, for any other normalized probability density $f \neq f_0$ the inequality $\Omega[f] > \Omega[f_0]$ holds:

$$\begin{aligned}\Omega[f] &= \mathrm{Tr}_{cl}\{f \cdot (H_N - \mu N + \beta^{-1} \ln f)\} \\ &= \mathrm{Tr}_{cl}\{f \cdot (\Omega[f_0] + \beta^{-1} \ln f - \beta^{-1} \ln f_0)\} \\ &= \Omega[f_0] + \beta^{-1}\mathrm{Tr}_{cl}\{f \cdot (\ln f - \ln f_0)\} \\ &> \Omega[f_0] \text{ for } f \neq f_0,\end{aligned} \quad , \tag{2.10}$$

in which the second equality uses $H_N - \mu N = \Omega[f_0] - \beta^{-1} \ln f_0$ which follows from Eq.(2.2), Eq.(2.7) and (2.9). The inequality in the last step is known as the Gibbs Inequality, a proof can be found in [3].

The equilibrium probability density f_0 is a function of $V_{ext}(\mathbf{r})$ and therefore the equilibrium density $\rho_0(\mathbf{r})$ is a *functional* of $V_{ext}(\mathbf{r})$ through Eq.(2.6). Because $V_{ext}(\mathbf{r})$ is uniquely determined by $\rho_0(\mathbf{r})$ for a given interaction potential $\Phi(\mathbf{r}_1 \cdots \mathbf{r}_N)$ and a given β, which is proved in [3], the equilibrium probability density f_0 is a functional of $\rho_0(\mathbf{r})$. This allows us to write $\Omega[f_0]$ as $\Omega[\rho_0]$ because it is now a functional of $\rho_0(\mathbf{r})$ through f_0.

Likewise, any normalized probability density $f \neq f_0$ is a functional of the corresponding equilibrium density $\rho(\mathbf{r})$ and we can rewrite the result $\Omega[f] > \Omega[f_0]$ as $\Omega[\rho] > \Omega[\rho_0]\ \forall\ \rho \neq \rho_0$.

The above can be condensed into

$$\left.\frac{\delta\Omega[\rho(\mathbf{r})]}{\delta\rho(\mathbf{r})}\right|_{\rho=\rho_0(\mathbf{r})} = 0 \quad \text{and} \quad \Omega[\rho_0] = \Omega. \tag{2.11}$$

We can define, for a given μ and $V_{ext}(z)$, the intrinsic Helmholtz free-energy functional

$$\mathcal{F}[\rho] = \Omega[\rho] - \int d\mathbf{r}\rho(\mathbf{r})(V_{ext}(\mathbf{r}) - \mu), \tag{2.12}$$

which is a functional of $\rho(\mathbf{r})$ and satisfies:

$$\left.\frac{\delta\mathcal{F}[\rho(\mathbf{r})]}{\delta\rho(\mathbf{r})}\right|_{\rho=\rho_0(\mathbf{r})} = \mu - V_{ext}(\mathbf{r}). \tag{2.13}$$

The Helmholtz free energy of the system is

$$F = \Omega + \mu N, \tag{2.14}$$

where $N = \int \rho_0(\mathbf{r})d\mathbf{r}$ and $\Omega = \Omega[\rho_0(\mathbf{r})]$. Substituting Eq.(2.12) for Ω yields

$$F = \mathcal{F}[\rho_0(\mathbf{r})] + \int d\mathbf{r}\rho_0(\mathbf{r})V_{ext}(\mathbf{r}), \tag{2.15}$$

which shows that the part of F that is 'intrinsic' to the system, that is, the energy not due to $V_{ext}(\mathbf{r})$, is indeed equal to $\mathcal{F}[\rho_0(\mathbf{r})]$ as the name suggests.

So instead of calculating the grand canonical partition function Ξ by analytical or numerical integration, which is impossible in either case, we can instead minimize the grand potential $\Omega[\rho(\mathbf{r})]$, or equivalently, solve the Euler-Lagrange equation that follows from the definition of $\mathcal{F}[\rho(\mathbf{r})]$ with respect to the density $\rho(\mathbf{r})$, to obtain the structure and properties of the system. Solving the Euler-Lagrange equation, provided $\mathcal{F}[\rho(\mathbf{r})]$ is known, presents no significant challenge to modern numerical methods, however, for almost all interaction potentials with the exception of the free ideal gas the expresion of $\mathcal{F}[\rho(\mathbf{r})]$ is unknown. The search for $\mathcal{F}[\rho(\mathbf{r})]$ given particles with interaction $\Phi\left(\mathbf{r}_1 \cdots \mathbf{r}_N\right)$ at temperature T, for example for hard spheres or Lennard-Jones particles, is an important problem in density functional theory[3].

It is convenient to split $\mathcal{F}[\rho(\mathbf{r})]$ into an ideal-gas contribution and an excess free-energy contribution due to particle-particle interactions:

$$\mathcal{F}[\rho(\mathbf{r})] = \mathcal{F}_{id}[\rho(\mathbf{r})] + \mathcal{F}_{exc}[\rho(\mathbf{r})], \tag{2.16}$$

where $\mathcal{F}_{id}[\rho(\mathbf{r})]$ is known[9] as:

$$\beta\mathcal{F}_{id}[\rho(\mathbf{r}] = \int d\mathbf{r}\rho(\mathbf{r}) \left(\ln \rho(\mathbf{r})\Lambda^3 - 1\right). \tag{2.17}$$

Here $\Lambda = h(2\pi k_B T m)^{-1/2}$ is the thermal wavelength. Differentiating both sides of Eq.(2.16) to $\rho(\mathbf{r})$ and involving Eq.(2.13) yields a self-consistency equation for the equilibrium density $\rho_0(\mathbf{r})$:

$$\Lambda^3\rho_0(\mathbf{r}) = \exp\left(\beta\mu - \beta\frac{\delta\mathcal{F}_{exc}[\rho(\mathbf{r})]}{\delta\rho(\mathbf{r})}\bigg|_{\rho=\rho_0(\mathbf{r})} - \beta V_{ext}(\mathbf{r})\right). \tag{2.18}$$

Because the one-body direct correlation function $c^{(1)}(\mathbf{r}) = -\beta\frac{\delta\mathcal{F}_{exc}[\rho(\mathbf{r})]}{\delta\rho(\mathbf{r})}$ is generally unknown unless $\mathcal{F}_{exc}[\rho(\mathbf{r})]$ is known, the above equation is not helpful, but it is the generative equation for iterations in a numerical minimization process, as will become clear later. Note that for an ideal gas, $\mathcal{F}_{exc}[\rho(\mathbf{r})] = 0$ and we recover

$$\rho_0(\mathbf{r}) = \rho_{bulk} \exp\left(-\beta V_{ext}(\mathbf{r})\right), \tag{2.19}$$

where $\rho_{bulk} = \frac{\exp(\beta\mu)}{\Lambda^3}$ is the equilibrium density of an ideal gas at chemical potential μ in the absence of an external field.

2.3 Hard spheres and the Rosenfeld functional

As touched upon in the introduction, the hard-sphere potential serves as a good reference system to model the repulsive part of many types of particle, such as Lennard-Jones particles. In 1989 Yasha Rosenfeld developed an approach to approximate the excess free-energy functional of hard spheres, famously known as the Fundamental Measure Theory (FMT)[3].

This approach, based on the geometrical properties of hard spheres, yields accurate results for most situations such as hard-sphere adsorption at a hard wall. Afterwards, improvements have been developed by Rosenfeld and Tarazona by requiring that the exact free energy in the zero-dimensional limit is recovered by this functional, and this new version of FMT also describes situations of extreme confinement such as hard-sphere freezing transitions well. The original Rosenfeld (RF) functional in $3D$ is of the form

$$\beta\mathcal{F}_{exc}^{RF}[\rho(\mathbf{r})] = \int d\mathbf{r}' \; \Phi^{RF}(\{n_\alpha(\mathbf{r}')\}), \tag{2.20}$$

where $\Phi^{RF}(\{n_\alpha(\mathbf{r}')\})$ is the reduced free-energy density; a function of weighted densities $n_\alpha(\mathbf{r})$:

$$\Phi^{RF}(\{n_\alpha(\mathbf{r})\}) = -n_0 \ln(1-n_3) + \frac{n_1 n_2 - \vec{n}_1 \cdot \vec{n}_2}{1-n_3} + \frac{n_2^3 - 3n_2 \vec{n}_2 \cdot \vec{n}_2}{24\pi(1-n_3)^2}. \tag{2.21}$$

The weighted densities are convolutions of the density $\rho(\mathbf{r})$ with certain scalar and vector weighting kernels $\omega_i(\mathbf{r})$ and $\vec{\omega}_i(\mathbf{r})$:

$$n_\alpha(\mathbf{r}) = \int d\mathbf{r}' \rho(\mathbf{r}') \omega_\alpha(\mathbf{r} - \mathbf{r}'). \tag{2.22}$$

The $\vec{n}_\alpha(\mathbf{r})$ are defined analogously. The weighting kernels are given[3] by:

$$\begin{aligned}
\omega_3(\mathbf{r}) &= \Theta(R - |\mathbf{r}|), \\
\omega_2(\mathbf{r}) &= \delta(R - |\mathbf{r}|), \\
\omega_1(\mathbf{r}) &= \frac{\omega_2(\mathbf{r})}{4\pi R}, \\
\omega_0(\mathbf{r}) &= \frac{\omega_2(\mathbf{r})}{4\pi R^2}, \\
\vec{\omega}_2(\mathbf{r}) &= \frac{\mathbf{r}}{|\mathbf{r}|}\delta(R - |\mathbf{r}|), \\
\vec{\omega}_1(\mathbf{r}) &= \frac{\vec{\omega}_2(\mathbf{r})}{4\pi R},
\end{aligned} \tag{2.23}$$

where R is the radius of the particle and $\Theta(..)$ and $\delta(..)$ denote the $3D$ Heaviside step function and Dirac delta function, respectively.

In this thesis we are solely concerned with planar geometries, that is, the external potential is only dependent on one coordinate, which we take to be z without loss of generality; $V_{ext}(\mathbf{r}) = V_{ext}(z)$. By symmetry, and in the absence of spontaneous symmetry breaking, the equilibrium density $\rho_0(\mathbf{r})$ is then homogeneous in x and y and therefore only dependent on z; $\rho_0(\mathbf{r}) = \rho_0(z)$. It is now possible to perform two of the three integrals in $n_\alpha(\mathbf{r})$ analytically so that

$$n_\alpha(\mathbf{r}) = n_\alpha(z) = \int dz' \rho(z') \omega_\alpha(z - z'), \tag{2.24}$$

and similarly for $\vec{n}_\alpha(z)$. The weighting kernels $\omega_\alpha(z)$ are now reduced to functions of a single variable and are given by:

$$\begin{aligned}
\omega_3(z) &= \pi(R^2 - z^2), \\
\omega_2(z) &= 2\pi R, \\
\omega_1(z) &= \frac{1}{2}, \\
\omega_0(z) &= \frac{1}{2R}, \\
\vec{\omega}_2(z) &= 2\pi z\hat{z}, \\
\vec{\omega}_1(z) &= \frac{z\hat{z}}{2R},
\end{aligned} \tag{2.25}$$

in which $\hat{z}$ is the outward-pointing unit vector perpendicular to the xy-plane.
Given some chemical potential μ and external potential $V_{ext}(z)$ we can use Eq.(2.18) to calculate the equilibrium density profile $\rho(z)$ of hard spheres. This requires the calculation of $c^{(1)}(z) = -\beta\frac{\delta\mathcal{F}_{exc}[\rho(\mathbf{r})]}{\delta\rho(\mathbf{r})}$, which is straightforwardly evaluated for hard spheres in planar geometries:

$$\begin{aligned}
c^{(1)}(z) &= -\int dz' \sum_i \frac{\partial\Phi^{RF}}{\partial n_i(z')}\frac{\delta n_i(z')}{\delta\rho(z)} \quad \text{with} \\
\frac{\delta n_i(z')}{\delta\rho(z)} &= \frac{\delta}{\delta\rho(z)}\int dz''\rho(z'')\omega_i(z'-z'') = \omega_i(z'-z),
\end{aligned} \tag{2.26}$$

so that finally

$$c^{(1)}(z) = -\sum_i \int dz' \frac{\partial\Phi^{RF}}{\partial n_i(z')}\omega_i(z'-z). \tag{2.27}$$

Here $\frac{\partial\Phi^{RF}}{\partial n_i(z')}$ is readily evaluated by partially differentiating Eq.(2.21) to n_i, and the sum is over both scalar- and vector weighting kernels alike. Note that in the latter expression we have $\omega_i(z'-z)$, instead of $\omega_i(z-z')$ as before, and the integral is therefore a cross-correlation (which we denote by $\otimes$), instead of a convolution:

$$c^{(1)}(z) = -\sum_i \left(\frac{\partial\Phi^{RF}}{\partial n_i} \otimes \omega_i\right)(z). \tag{2.28}$$

Eq.(2.28) allows (numerical) calculation of the equilibrium density $\rho_0(z)$ by involving Eq.(2.18), for some given μ, β and $V_{ext}(z)$. This can be done by the so-called Picard iteration method. First a guess is required for $\rho_0(z)$, which can simply be taken as $\rho^0(z) = \rho^0 \exp\left(-V_{ext}(z)\right)$ for some constant $\rho^0 \in (0, \sigma^{-3})$. Then $c^{(1)}(z)$ is evaluated for $\rho_0(z)$ and inserted in Eq.(2.18), which yields a new density profile $\rho^1(z)$, and the process is repeated which yields $\rho^2(z), \rho^3(z), \rho^4(z)...$ until the successive differences between $\rho^k(z)$ and $\rho^{k+1}(z)$ are below some pre-defined threshold value. The last iteration's result is then taken to be the equilibrium density profile $\rho_0(z)$.

2.4 The Lennard-Jones potential and mean field theory

The Lennard-Jones 12-6 interaction potential is given[1] by

$$U(r) = 4\epsilon\left(\left(\frac{\sigma}{r}\right)^{12} - \left(\frac{\sigma}{r}\right)^{6}\right), \tag{2.29}$$

where $r = |\mathbf{r}|$, and where σ is the particle diameter. The r^{-6} term describes the long-range attractive Van der Waals forces between neutral pairs of atoms or small molecules and the r^{-12} term describes the short-range repulsion. The exponent of the latter term has no physical meaning, but is simply a convenient choice. The minimum value of the potential is $-\epsilon$ which occurs at $r = r_m = 2^{1/6}\sigma$. A plot of the Lennard-Jones potential of Eq.(2.29) is given in Figure 2.1.

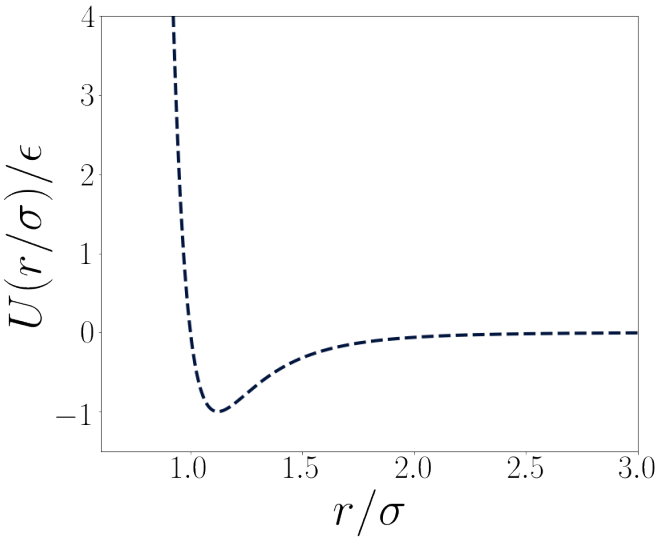

Figure 2.1: The Lennard-Jones 12-6 interaction potential of Eq.(2.29).

We can split the Lennard-Jones potential into an attractive and a repulsive part so that $U(r) = U_{rep}(r) + U_{att}(r)$. We employ the Barker-Henderson splitting, which is[11] simply:

$$U_{rep}(r) = \begin{cases} U(r), & \text{if } r \leq \sigma \\ 0, & \text{otherwise,} \end{cases} \tag{2.30}$$

and

$$U_{att}(r) = \begin{cases} 0, & \text{if } r \leq \sigma \\ U(r), & \text{otherwise.} \end{cases} \tag{2.31}$$

Here $U_{rep}(r)$ is modelled by hard spheres with an effective diameter d (generally not equal to σ), where the temperature dependence of d was derived by Barker and Henderson[11]. An approximation (see [11]) is

$$\frac{d}{\sigma} = \frac{1 + 0.2977T^*}{1 + 0.33163T^* + 1.0477 \cdot 10^{-3}T^{*2}}, \tag{2.32}$$

where $T^* = k_b T/\epsilon = 1/\epsilon^*$ is the so-called reduced temperature. This approximation works well in the range of $T^* \in (0, 15)$.

We can therefore split the excess free-energy functional for the Lennard-Jones 12-6 system into a repulsive part modelled by the Rosenfeld functional for hard spheres with diameter d, and an attractive part, so that

$$\mathcal{F}_{exc}^{LJ}[\rho(\mathbf{r})] = \mathcal{F}_{exc}^{RF}[\rho(\mathbf{r}); d] + \mathcal{F}_{exc}^{att}[\rho(\mathbf{r})]. \tag{2.33}$$

A crude approximation for the attractive part is the mean field approximation[8]

$$\mathcal{F}^{MF}[\rho(\mathbf{r})] = \frac{1}{2}\int\int d\mathbf{r}d\mathbf{r}'\rho(\mathbf{r})\rho(\mathbf{r}')U_{att}(|\mathbf{r}-\mathbf{r}'|). \tag{2.34}$$

In the rest of this thesis we denote this mean field theory approximation for $\mathcal{F}_{exc}^{att}[\rho(\mathbf{r})]$ as MF.
In planar geometries, $\rho(\mathbf{r}) = \rho(z)$, and

$$\mathcal{F}^{MF}[\rho(z)] = \frac{1}{2}\int\int dzdz'\rho(z)\rho(z')U_{att,z}(|z-z'|), \tag{2.35}$$

where we scaled out the factor ϵ and introduced the dimensionless xy-integrated attractive part of the LJ-potential

$$\begin{aligned} U_{att,z}(z) &= \int_{-\infty}^{\infty}\int_{-\infty}^{\infty}\frac{U_{att}(\sqrt{x^2+y^2+z^2})}{\epsilon}dxdy \\ &= \begin{cases} -\dfrac{6\pi\sigma^2}{5}, & \text{if } |z| \le \sigma \\ \dfrac{2\pi\sigma^6(2\sigma^6 - 5z^6)}{5z^{10}}, & \text{if } |z| > \sigma. \end{cases} \end{aligned} \tag{2.36}$$

This result is derived in Appendix A.1. In Figure 2.2 $U_{att}(z)$ is plotted.

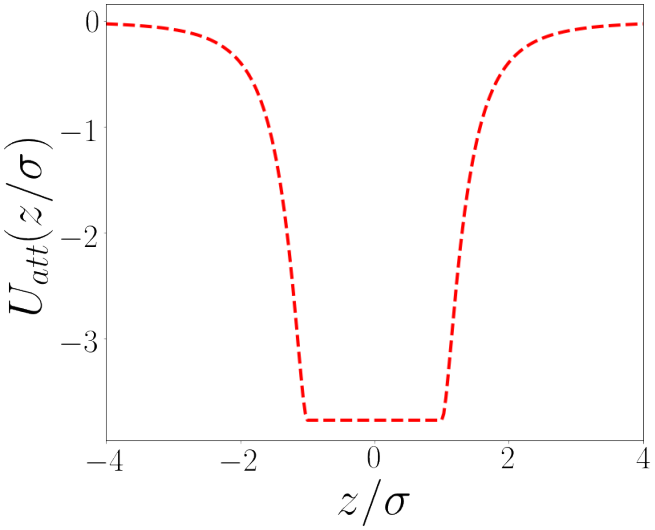

Figure 2.2: The integrated mean field kernel $U_{att}(z)$ of Eq.(2.36).

The one-body direct correlation function $c^{(1)}(z)$ for the Lennard-Jones potential in the mean-field approximation then follows straightforwardly:

$$\begin{aligned} c^{(1,LJ)}(z) = -\beta \frac{\delta \mathcal{F}_{exc}^{LJ}[\rho(z)]}{\delta \rho(z)} &= -\beta \left(\frac{\delta \mathcal{F}_{exc}^{RF}[\rho(z); d]}{\delta \rho(z)} + \frac{\delta \mathcal{F}^{MF}[\rho(z)]}{\delta \rho(z)} \right) \\ &= c^{(1,RF)}(z) - \beta \Big(\rho * U_{att,z} \Big)(z) \end{aligned} \tag{2.37}$$

with $c^{(1,RF)}(z)$ given by Eq.(2.28) and $*$ denoting convolution. Given an external potential $V_{ext}(z)$, chemical potential μ and (inverse) temperature β the equilibrium density profile $\rho_0(z)$ can then be approximated by applying Picard iteration on Eq.(2.18) as described at the end of Section 2.3.

3 Methodology

3.1 Introduction to the method used

In this thesis we use ML to construct a better attractive excess free-energy functional $\mathcal{F}^{att}_{exc}[\rho(\mathbf{r})]$ for the attractive part of the Lennard-Jones 12-6 potential in planar geometries in $3D$. We aim to improve the mean-field approximation given by Eq.(2.34). Here we briefly give an overview of the method used and then explain each component more in-depth in the corresponding subsection below.

To use ML to construct a better functional in the first place, two things are essential: Training data and an Ansatz for the functional. With 'training data' we mean an information set of which each element has the form $((\mu, V_{ext}(z)), (\rho(z))$ where $\rho(z)$ is the *true* equilibrium density distribution that would be found in a system with chemical potential μ and external potential $V_{ext}(z)$. Because the true functional $\mathcal{F}[\rho(\mathbf{r})]$ is certainly independent of μ and $V_{ext}(z)$[9], but cannot be proven to be independent of the (reduced) interaction energy $\epsilon^* = \beta\epsilon$ (not of either ϵ or β to be precise), training data should consist of varying μ and $V_{ext}(z)$ for a fixed ϵ^*. This way, the functional is constructed for that specific ϵ^*.

Therefore, the idea is, for some fixed ϵ^*, to construct a functional that minimizes the discrepancy between the output densities $\rho_i^{ML}(z)$ it produces for some $(\mu, V_{ext}(z))_i$ and the *true* densities $\rho_i(z)$ corresponding to this $(\mu, V_{ext}(z))_i$. The *true* densities can be approximated to very high accuracy with Monte Carlo (MC) simulations, which is one of the most heavily used type of simulation in the field of computational soft condensed matter theory[10]. MC is used in this thesis and we elaborate on the precise simulation method and settings in the next subsection.

What exactly is meant by 'minimizing the discrepancy' (in ML language: minimizing the loss) between the output densities and the true densities is a point of discussion. We treat the MC-simulated densities as 'exact', and an ML functional will always yield the same resulting output density for some input μ and $V_{ext}(z)$, that is, it is not a random variable. This means that there is no probabilistic aspect at all to this model, and hence there is no direct incentive to use any statistical estimation method such as Ordinary Least Squares or Maximum Likelihood Estimation above any other method[12].

However, it turns out to be the most convenient, when implementing the training process, to minimize a squared-difference type loss function. First due to the convexity of the loss function not requiring special measures to prevent negative loss, and second due to the computationally convenient linear first derivative of the loss function with respect to the densities. To be precise, based on the same approach as in [8], we minimize the criterion:

$$J = \sum_i \int dz (\rho_i^{MC}(z) - \rho_i^{ML}(z))^2, \tag{3.1}$$

where the sum is over the entire training data set and the integral over the length of the simulated system.

Second to training data, we need an *Ansatz* for the functional in terms of some unknown parameters β_i and / or weighting kernels $\omega_i(z)$ so that we can minimize the loss function J *with respect to* these parameters and / or weighting kernels. It is non-trivial to conjure up a good Ansatz because we do not know what the mathematical form of the true functional $\mathcal{F}^{att}_{exc}[\rho(\mathbf{r})]$ is. Furthermore, care must be taken not to utilize too many weighting kernels and / or parameters, as this can easily cause overfitting and bad out-of-sample predictions[6].

3.2 Data generation

We use grand canonical MC simulations to generate data. A box (x, y, z) defined by $x \in (0, 16\sigma)$, $y \in (0, 16\sigma)$, $z \in (0, 8\sigma)$ is chosen as the system under consideration, and the particle diameter σ is taken to be the unit of length. We employ periodic boundary conditions in each dimension, and use the nearest-image convention, that is, each particle i only interacts with that particle j that is nearest to it when the system is copied next to itself in each direction.

The Lennard-Jones potential in the simulation is truncated at $r = r_{cut} = 2.5\sigma$ and a correction $e_{cut} = 4\epsilon((\frac{\sigma}{r_{cut}})^{12} - (\frac{\sigma}{r_{cut}})^{6})$ is substracted from each particle-particle interaction energy to remove the discontinuity in the potential, an approach based on [10]. The system is divided into cubic cells with length equal to r_{cut}, so that each particle only interacts with particles in neighbouring cells (including cells of 'image' systems). This is not a further approximation, but simply an optimization method.

3.2.1 Generating the training data set

Each simulation in the training data set is done for some pre-defined chemical potential μ and external potential $V_{ext}(z)$. The (reduced) interaction energy ϵ^* is the same for all simulations because, as we already mentioned, the functional may be dependent on the temperature or the interaction energy, and hence we train for only a single ϵ^*. The chemical potentials used are $\mu^* = \beta\mu \in \{-1.5, -0.5, 0.0, 0.5, 1.5\}$, which for $\epsilon^* = 0.5$ correspond to bulk densities of respectively $\rho\sigma^3 \in \{0.268, 0.490, 0.565, 0.624, 0.710\}$. The external potentials are all of the same mathematical form as in [8], namely:

$$\beta V_{ext}(z) = \begin{cases} a((\frac{L_z/\sigma}{2} - b(L_z/\sigma)) - z/\sigma)^c, & \text{if } z/\sigma < \frac{L_z/\sigma}{2} - b(L_z/\sigma) \\ a(z/\sigma - (\frac{L_z/\sigma}{2} + b(L_z/\sigma)))^c, & \text{if } z/\sigma > \frac{L_z/\sigma}{2} + b(L_z/\sigma) \\ 0, & \text{otherwise.} \end{cases} \tag{3.2}$$

The parameters (a, b, c) vary per simulation and are all the possible combinations of $a \in \{3.0, 6.0, 9.0\}$, $b \in \{0.15, 0.20, 0.25, 0.30, 0.35\}$, $c \in \{2.0, 3.0, 4.0\}$. So in total the training set consists of $5 \cdot 3 \cdot 5 \cdot 3 = 225$ MC simulations. Furthermore, L_z is the box size in the z-direction, we use $L_z = 8\sigma$. It can easily be verified that all $\beta V_{ext}(z)$ are symmetric about $z = \frac{L_z}{2}$. This is convenient because, by symmetry, the true densities $\rho(z)$ should then be symmetric as well

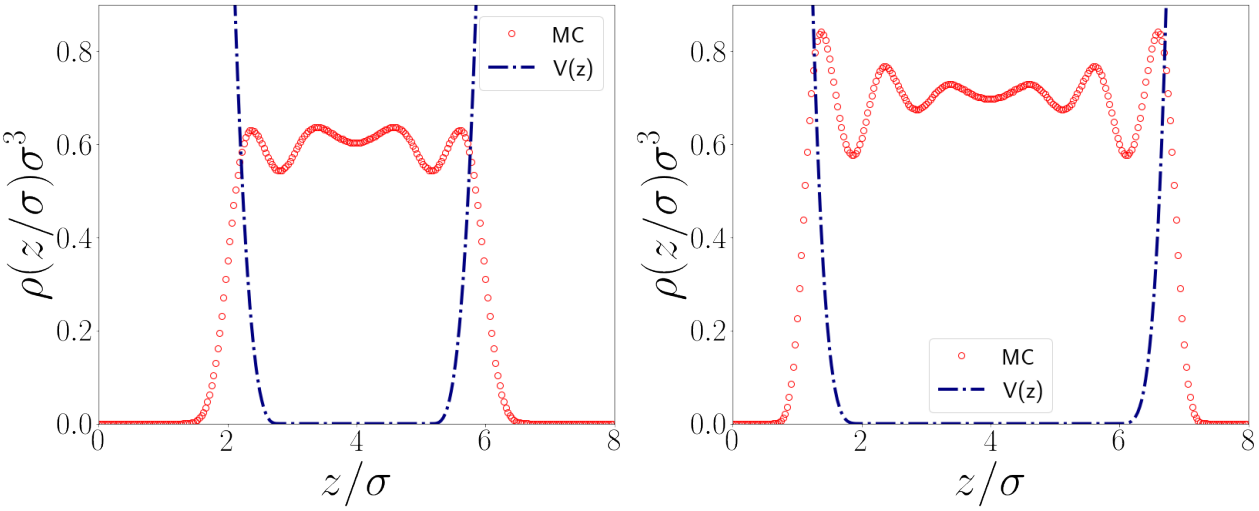

(a) $\mu^* = 0.5$, $V(z)$ with $a = 3.0$, $b = 0.15$ and $c = 3.0$.

(b) $\mu^* = 1.5$, $V(z)$ with $a = 3.0$, $b = 0.25$ and $c = 4.0$.

Figure 3.1: Two MC simulations for different external potentials $V(z)$ (dark blue dot-dashed line) and different chemical potentials μ. The red open circles are the MC-simulated density profile. Both simulations are for $\epsilon^* = 0.5$.

and this yields us extra information which we can use to double the accuracy of the simulations. In $\beta V_{ext}(z)$, the parameter a simply represents a multiplicative factor for the energy, b is the fraction of the distance between the center of the box and the onset of the external potential, and c represents the steepness of the potential as the system boundaries are neared.

An MC simulation in our method consists of 10^6 MC 'cycles'. In each cycle a so-called trial move is performed N times, where N denotes the current amount of particles in the system. A trial move consists of either an attempt to move a particle that is already in the system, or an attempt to insert a particle at a random position in the system or delete a random particle. An attempt to move a particle is made with probability 0.9 and an attempt to either insert or delete a particle with probability 0.1. These probabilities are arbitrary but appear to work sufficiently well to quickly equilibrate the system, as we determined by comparison with other values, and we also noted that the end result in a large simulation is the same either way.
When an attempt to move a particle is made, a random particle is chosen, together with three random real numbers in the range $(-\delta, \delta)$ which represent the particle's move in each direction. Here δ is chosen so that a move is accepted with probability approximately equal to 0.5, where $\delta = 0.1$ often works well but can be made to vary during the simulation. Periodic boundary conditions make sure that the particle stays in the system at all times. The difference in energy $\Delta U = U_{new} - U_{old}$ is computed and thereafter the acceptance rule[10]

$$acc(\text{old} \to \text{new}) = \min(1, \exp(-\beta \Delta U)). \tag{3.3}$$

Next a random real number $p \in (0, 1)$ is drawn. If $p < acc(\text{old} \to \text{new})$ the move is accepted, otherwise the move is rejected and the system is reset to its old configuration.

These rules are derived in [10]. When an attempt at either particle insertion or deletion is made, insertion is attempted with probability 0.5 and otherwise deletion is chosen. For insertion, a particle is inserted at a random position in the system and the difference ΔU between the new and old configuration is computed. For deletion, a random particle is deleted and the energy difference ΔU is computed. In either case, the respective acceptance rule is computed and the trial move is accepted when a random number $p \in (0, 1)$ drawn is of lower value than this rule. The acceptance rule for insertion is:

$$acc(N \to N+1) = \min(1, \frac{V}{\Lambda^3(N+1)} \exp\left(-\beta(\Delta U - \mu)\right), \tag{3.4}$$

and for deletion it is:

$$acc(N \to N-1) = \min(1, \frac{\Lambda^3 N}{V} \exp\left(-\beta(\Delta U + \mu)\right). \tag{3.5}$$

Here we set the thermal wavelength Λ equal to σ as is done in [10]. Before the density distribution gets sampled, the system is equilibrated by 10^4 MC cycles. After equilibrating the system, the density $\rho^{MC}(z)$ is sampled each fourth cycle, so that samples are decorrelated sufficiently, like was done in [8]. Therefore the equilibrium density distribution is sampled approximately $2.5 \cdot 10^5$ times. To sample the density, the system is divided in the z-direction by planar grids, with a width corresponding to 32 grids per particle diameter. This can be thought of as slicing up the system like cheese. Then the number of particles in each grid is divided by the volume of that grid and the resulting density is stored. At the end of the simulation, the average density is computed for each grid and can then be plotted and used for ML purposes. In Figure 3.1 two examples of MC-simulated density profiles are given for $\epsilon^* = 0.5$.

3.2.2 Generating the equation of state

We also use MC to simulate the equation of state for the bulk density $\rho_{bulk}(\mu)$ as a function of the chemical potential μ and the pressure $P(\rho)$ as a function of the density ρ. This is done so we can compare the predicted equation of state of ML to the MC data. The equation of state for the bulk density is easy to generate with MC, and, for a fixed chemical potential μ and (inverse) temperature ϵ^*, simply comes down to dividing the number of particles in the system by the system's volume in each MC cycle, and then taking the average over all cycles.

To calculate the pressure with MC, we use the virial equation of state[10]

$$\begin{aligned} \langle P \rangle &= \rho k_b T + \frac{1}{3V} \left\langle \sum_{i<j} \mathbf{f}(\mathbf{r_{ij}}) \cdot \mathbf{r_{ij}} \right\rangle \\ &= \rho k_b T + \frac{8\epsilon}{V} \left\langle \sum_{i<j} \left(2 \left(\frac{\sigma}{r_{ij}} \right)^{12} - \left(\frac{\sigma}{r_{ij}} \right)^{6} \right) \right\rangle, \end{aligned} \tag{3.6}$$

where the second equality follows from Eq.(2.29) and from the fact that the interparticle force $\mathbf{f}(\mathbf{r_{ij}})$ is parallel to the displacement vector $\mathbf{r_{ij}}$. The average is over all MC cycles, and the density ρ in Eq.(3.6) follows from the equation of state $\rho_{bulk}(\mu)$.

3.3 The training process illustrated for a simple case

A very simple Ansatz for the attractive part, based on mean field theory, is the functional:

$$\mathcal{F}^{att}[\rho(z)] = \frac{\epsilon}{2}\int\int dzdz'\rho(z)\rho(z')\omega_2(|z-z'|), \tag{3.7}$$

where $\omega_2(z)$ is to be determined by ML. We use a cutoff range of 8σ for $\omega_2(z)$ so that its domain is $[-4\sigma, 4\sigma]$. The subscript 2 is to emphasize that the corresponding term is of second order in the density. Because we use the Rosenfeld functional Eq.(2.21) to model the repulsive part of the potential, the complete Ansatz is therefore:

$$\mathcal{F}_{exc}^{LJ,ML}[\rho(z)] = \mathcal{F}^{RF}[\rho(z);d] + \mathcal{F}^{att}[\rho(z)] \tag{3.8}$$

The effective hard-sphere diameter d for the Rosenfeld functional is given by Barker and Henderson in Eq.(2.32).

We illustrate the training process for this Ansatz. The case $\omega_2(z) = U_{att,z}(z)$ with $U_{att,z}(z)$ defined in Eq.(2.36) is equivalent to MF. The loss J is to be minimized with respect to $\omega_2(z)$, which can be done by gradient descent. First we require an initial guess which we naturally take as $\omega_2^0(z) = U_{att,z}(z)$, that is, we initiate the learning process from mean field theory itself. Then we compute $\frac{\delta J}{\delta\omega_2(z)}|_{\omega_2(z)=\omega_2^0(z)}$ and update the kernel $\omega_2(z)$ to $\omega_2^1(z) = \omega_2^0(z) - \alpha\frac{\delta J}{\delta\omega_2(z)}|_{\omega_2(z)=\omega_2^0(z)}$ with $\alpha \in (0,1)$ some suitably choosing *learning rate*. So in general we repeat:

$$\omega_2^{k+1}(z) = \omega_2^k(z) - \alpha(k)\frac{\delta J}{\delta\omega_2(z)}\bigg|_{\omega_2(z)=\omega_2^k(z)}, \tag{3.9}$$

until the squared difference $\int dz(\omega_2^{k+1}(z)-\omega_2^k(z))^2$ is below some pre-defined threshold value, and where the learning parameter $\alpha(k)$ can in general be defined as a function of the iteration number k, which is called a *learning schedule*. We compute the functional derivative by involving Eq.(2.37) and noting that the MC densities $\rho_i^{MC}(z)$ are constant; they obviously do not depend on $\omega_2(z)$ and are fixed. The dependence on $\omega_2(z)$ is through $\rho_i^{ML}(z)$, which are generated by Eq.(2.18), the generative equation, repeated below for convenience:

$$\begin{aligned}\sigma^3\rho_{i,k}^{ML}(z) &= \exp\left(\beta\mu - \beta\frac{\delta\mathcal{F}_{exc}^{LJ}[\rho(z)]}{\delta\rho(z)}\bigg|_{\rho=\rho_i^{MC}(z)} - \beta V_{ext}(z)\right)\\ &= \exp\left(\beta\mu - \left(c^{(1,RF)}(z) - \epsilon^*(\rho_i^{MC} * \omega_2^k)(z)\right) - \beta V_{ext}(z)\right),\end{aligned} \tag{3.10}$$

where we use $\rho_{i,k}^{ML}(z)$ to denote the density for data set i generated by the ML functional in iteration k of the training process, and where $c^{(1,RF)}(z)$ is again the one-body direct correlation function of hard spheres as defined in Eq.(2.28). The star $*$ denotes convolution, opposed to cross-correlation as used earlier. However, due to the symmetry of the weighting kernels, cross-correlation and convolution yield equal results. Also note that we evaluate the functional derivative $\frac{\delta\mathcal{F}_{exc}^{LJ}[\rho(z)]}{\delta\rho(z)}\Big|_{\rho=\rho_i^{MC}(z)}$ on the MC densities and do not numerically solve the

Euler-Lagrange equation Eq.(2.18) each time, this is done to accelerate the training process.

Using Eq.(3.10) we compute $\frac{\delta J}{\delta\omega_2(z)}|_{\omega_2(z)=\omega_2^k(z)}$:

$$\begin{aligned}\left.\frac{\delta J}{\delta\omega_2(z')}\right|_{\omega_2(z)=\omega_2^k(z)} &= -2\sum_i \int dz(\rho_i^{MC}(z)-\rho_{i,k}^{ML}(z))\left.\frac{\delta\rho_{i,k}^{ML}(z)}{\delta\omega_2(z')}\right|_{\omega_2(z)=\omega^k(z)} \\ &= -2\epsilon^*\sum_i \int dz(\rho_i^{MC}(z)-\rho_{i,k}^{ML}(z))\rho_{i,k}^{ML}(z)\rho_i^{MC}(z'+z),\end{aligned} \tag{3.11}$$

which follows by applying the chain rule and using that

$$\frac{\delta(\rho_i^{MC}*\omega_2)(z)}{\delta\omega_2(z')} = \rho_i^{MC}(z'+z). \tag{3.12}$$

So the training process for the above mean field-like case can be summarized as:

1. Start with a guess for $\omega_2(z)$, for example $\omega_2^0(z) = U_{att,z}(z)$. For numerical implementation, $\omega_2(z)$ should be discretised on a pre-defined grid, with grid spacing equal to the one used in the MC simulations.
2. Compute all $\rho_{i,0}^{ML}(z)$ by Eq.(3.10).
3. Compute $\frac{\delta J}{\delta\omega_2(z')}|_{\omega_2(z)=\omega_2^0(z)}$ by Eq.(3.11).
4. Compute the new $\omega_2^1(z)$ by Eq.(3.9).
5. Repeat step 2, 3 and 4 for each next iteration k until convergence is reached.

The process for any other *Ansatz* for $\mathcal{F}^{att}[\rho(z)]$ is analogous, however, of course, when more parameters and / or weighting kernels are used, the loss J should be minimized with respect to *all* parameters and kernels, and each iteration involves differentiating J with respect to all parameters and kernels to be determined, and these derivatives generally depend on one another. Furthermore, as the Ansatz becomes more complex, the derivatives become mathematically much more involved. Nevertheless, the main reasoning remains the same.

3.4 Making predictions with ML

When the training process is finished and the ML functional is constructed for a certain temperature, we can make predictions with ML such as computing the density profile for arbitrary μ and $V(z)$, and computing the equation of state. To compute a density profile, the Euler-Lagrange equation

$$\sigma^3\rho^{ML}(z) = \exp\left(\beta\mu - \beta\left.\frac{\delta\mathcal{F}_{exc}^{LJ,ML}[\rho(z)]}{\delta\rho(z)}\right|_{\rho^{ML}(z)} - \beta V_{ext}(z)\right. \tag{3.13}$$

is solved by the Picard iteration method described in Section 2.3. To generate the equation of state $\rho_{bulk}(\mu)$, Eq.(3.13) is solved with $V_{ext}(z) = 0$ for the desired range of μ. To compute the equation of state for the pressure $P(\rho)$, the Gibbs-Duhem equation[9]

$$\begin{aligned} N d\mu &= -SdT + VdP, \\ \rho(\mu) d\mu &= dP, \\ \int_0^P dP' &= \int_{-\infty}^{\mu} \rho(\mu') d\mu', \\ P(\mu) &= \int_{-\infty}^{\mu} \rho(\mu') d\mu' \end{aligned} \tag{3.14}$$

is used, where the second equality follows from $dT = 0$ in the grand canonical ensemble. The relation $P(\mu)$ can then be cast into $P(\rho)$ by inverting the equation of state $\rho(\mu)$ computed before. Because for low μ the system behaves like an ideal gas, the first part of the integral $\int_{-\infty}^{\mu_{min}} \rho(\mu') d\mu'$ can be done analytically by invoking the ideal gas law $\rho = \frac{\exp(\mu^*)}{\Lambda^3}$, where μ_{min} denotes the smallest μ for which $\rho(\mu)$ was computed by ML.

4 Results

4.1 A mean-field like Ansatz

For a fixed temperature corresponding to $\epsilon^* = 0.5$ (or equivalently, $T^* = k_B T/\epsilon = 1/\epsilon^* = 2.0$), we start with a mean-field like Ansatz. Note that this temperature is well above the critical temperature $T_c^* = 1.188$ of the 2.5σ-truncated Lennard-Jones potential[13]. The training data set used is that of Section 3.2.1, where the external potential parameters a, b, c vary as well as the chemical potential μ. The Ansatz is

$$\mathcal{F}^{att}[\rho(z)] = \frac{\epsilon}{2} \int \int dz dz' \rho(z)\rho(z')\omega_2(|z - z'|). \tag{4.1}$$

The resulting kernel $\omega_2(z)$ is shown in Figure 4.1 together with the mean-field kernel of Eq.(2.36). With 'ML2' we mean ML with an Ansatz of second order in the density, as in Eq.(4.1). Apparently MF underestimates the attractive potential between particles with z-coordinates z and z' with $|z-z'| < \sigma$ and slightly overestimates the attraction for $|z-z'| > \sigma$. It is unclear how exactly the shape of $\omega_2(z)$ should be interpreted.

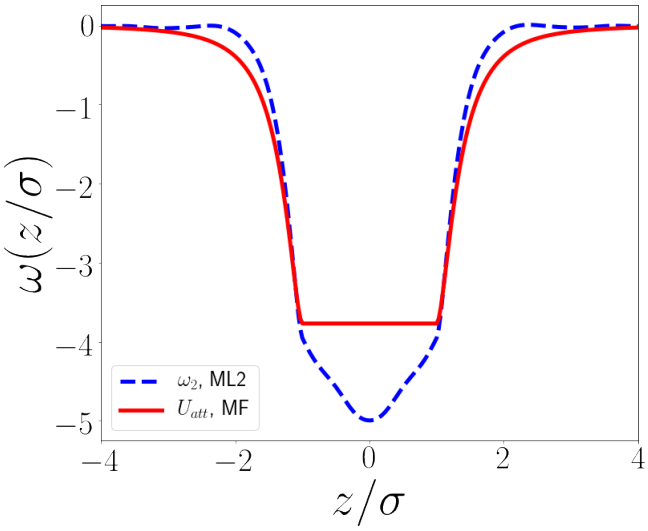

Figure 4.1: The trained mean-field like kernel $\omega_2(z)$ of Eq.(4.1) compared to the MF-kernel Eq.(2.36).

In Figure 4.2 the predicted density profiles of ML of a Lennard-Jones fluid between two planar hard walls are shown, together with the predicted density of MF Eq.(2.35), for $\mu^* = 0.0$ and $\mu^* = 0.75$. These hard-wall potentials were not part of the training set for ML and are therefore predictions. Clearly MF does not predict the bulk density well, in contrast to ML. Furthermore, the predicted density profile of ML appears to be more oscillatory which is in better agreement with the MC data.

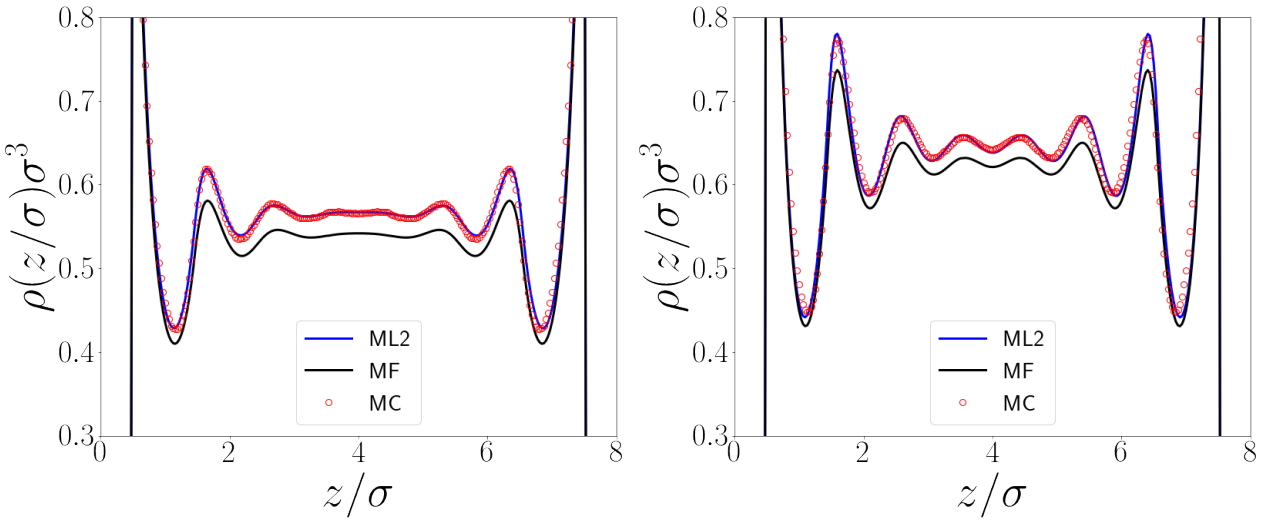

(a) At $\mu^* = 0.0$ ($\rho_{bulk} = 0.57$). (b) At $\mu^* = 0.75$ ($\rho_{bulk} = 0.64$).

Figure 4.2: A Lennard-Jones fluid between two planar hard walls at $\epsilon^* = 0.5$. The blue solid line is the prediction of ML with Ansatz Eq.(4.1), the black solid line the result of MF and the red open circles are the MC data. Not the entire plot range is shown.

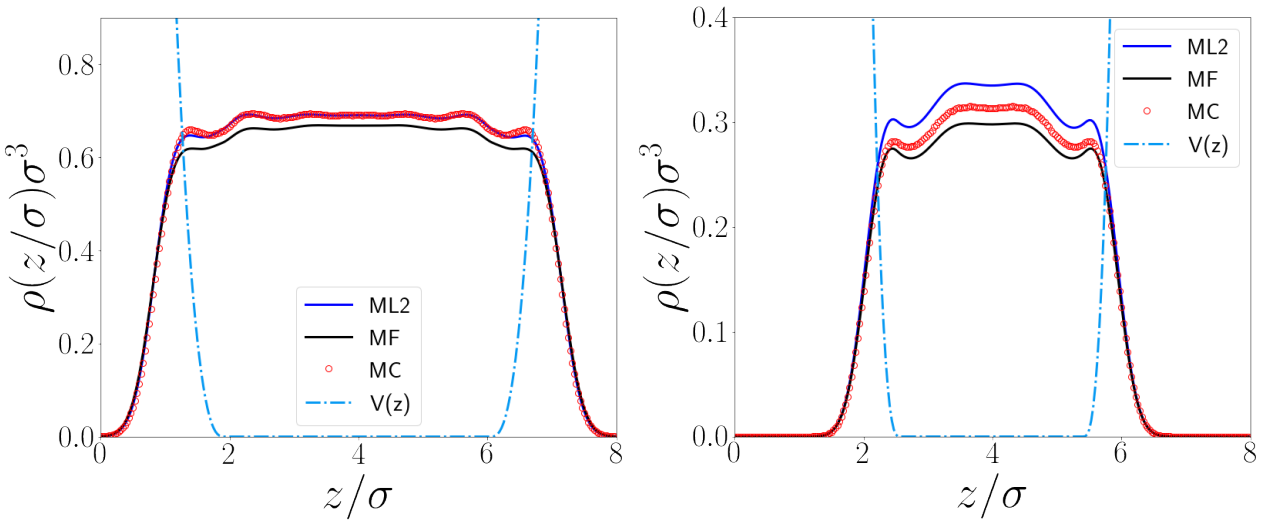

(a) At $\mu^* = 1.25$ ($\rho_{bulk} = 0.69$). The $V(z)$ used has parameters $a = 2.0, b = 0.26, c = 2.5$.

(b) At $\mu^* = -12.5$ ($\rho_{bulk} = 0.32$). The $V(z)$ used has parameters $a = 4.0, b = 0.18, c = 2.5$.

Figure 4.3: The predicted density profiles of ML and MF for two different external potentials $V(z)$ and chemical potentials μ that were not part of the training set. The blue dot-dashed line is the external potential $V(z)$ used.

In Figure 4.3 the predicted density profiles for two out-of-sample situations are shown, with different $V(z)$ and μ that were not part of the training set. ML predicts the case of $\mu^* = 1.25$ accurately but fails the predicted the low bulk density at $\mu^* = -1.25$, although the shape of the density profile seems to better than that of MF. MF underestimates the bulk density in both cases.

4.2 An Ansatz with an additional term of fourth order in the density

To improve on the previous Ansatz, we consider an extra kernel in addition to Eq.(4.1), resulting in

$$\mathcal{F}^{att}[\rho(z)] = \frac{\epsilon}{2}\int\int dzdz'\rho(z)\rho(z')\omega_2(|z-z'|) + \frac{\epsilon}{2}\int\int dzdz'\rho^2(z)\rho^2(z')\omega_4(|z-z'|). \quad (4.2)$$

The resulting kernels, for $\epsilon^* = 0.5$, are depicted in Figure 4.4. With 'ML2+4' we mean ML with an Ansatz of second and fourth order in the density, as in Eq.(4.2). The new $\omega_2(z)$ is slightly less attractive compared to the one of Eq.(4.1). The new kernel $\omega_4(z)$ is slightly negative inside the 'core' $|z-z'| < \sigma$ and slightly positive elsewhere.

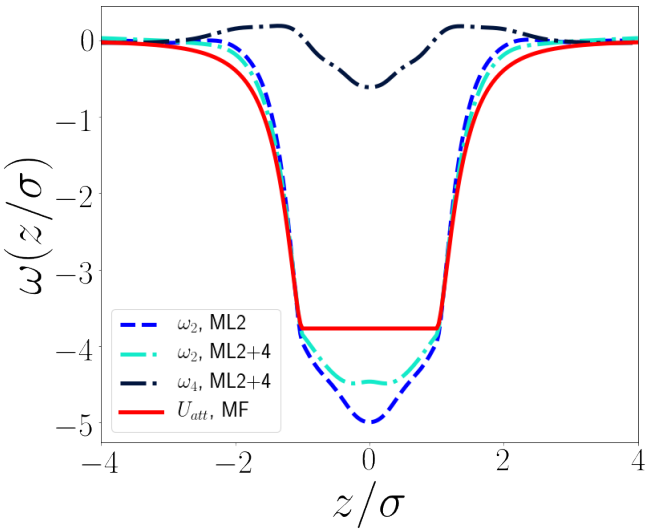

Figure 4.4: The trained kernels $\omega_2(z)$ and $\omega_4(z)$ of Eq.(4.2), together with the kernel of Eq.(4.1) and the MF-kernel Eq.(2.36).

In Figure 4.5 the predicted equation of state for $\rho_{bulk}(\mu)$ and $P(\rho)$ is shown. The Ansatz of Eq.(4.1) overestimates the density and hence the pressure for $\mu^* \in (-2.0, -0.5)$, that is, slightly above the ideal-gas regime. The new Ansatz of Eq.(4.2) performs somewhat better in this range although the agreement with MC data is still worse than that of MF. ML predicts higher densities and pressures better than MF, the latter underestimates those. In Figure

4.6 the differences $\Delta\rho = \rho - \rho_{MC}$ and $\Delta P = P - P_{MC}$ with the MC data are shown to better illustrate the relative performance of ML and MF.

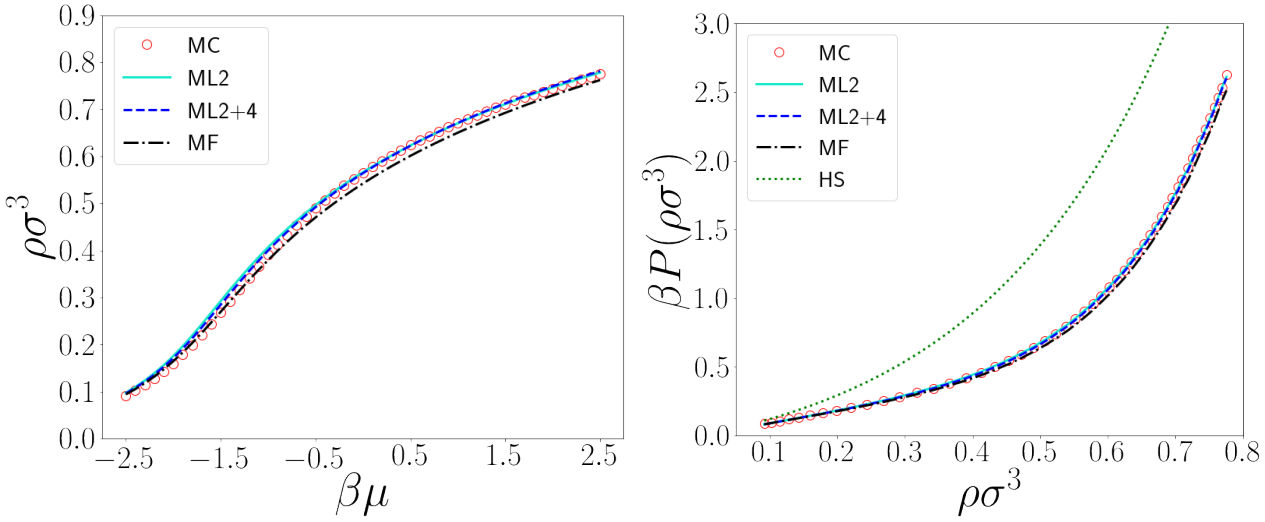

(a) The equation of state for $\rho_{bulk}(\mu)$.

(b) The equation of state for $P(\rho)$.

Figure 4.5: The equation of state. The light blue solid line is the result of ML with Ansatz Eq.(4.1), the blue dashed line the result of ML with Ansatz. Eq.(4.2), the black dot-dashed line the result of MF and the red open circles are the MC data. We also plotted the pressure for hard spheres (Carnahan-Starling) in green dots.

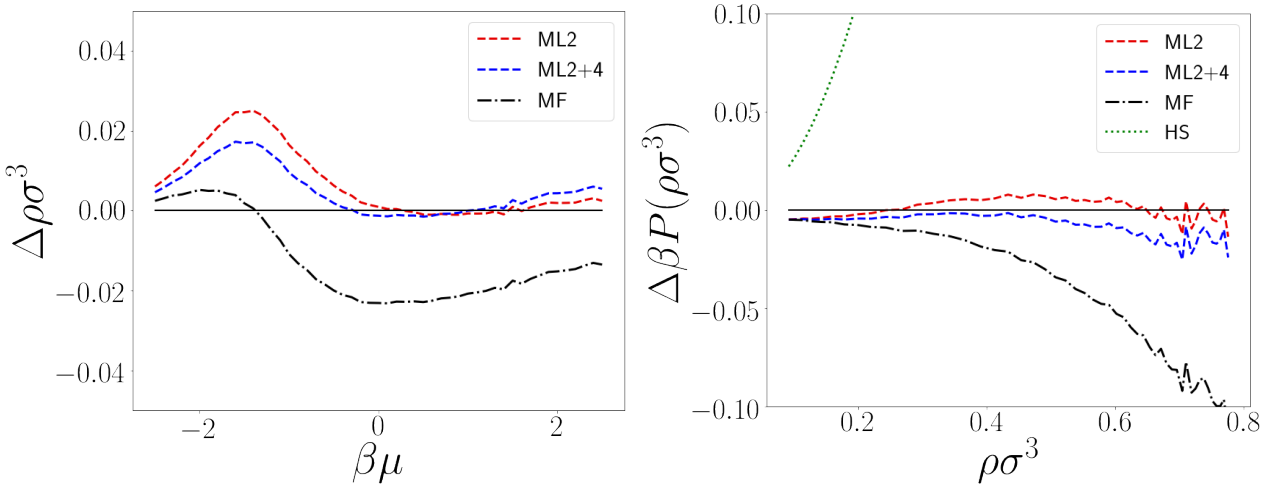

(a) Error in the predicted $\rho_{bulk}(\mu)$.

(b) Error in the predicted $P(\rho)$.

Figure 4.6: The errors compared to MC data for the equation of state, in terms of $\Delta\rho = \rho - \rho_{MC}$ and $\Delta P = P - P_{MC}$.

In Figure 4.7 we show two predicted density profiles, respectively for the case two planar hard walls at $\mu^* = 0.0$, and an external potential that was not in the training set at $\mu^* = 1.25$. We also computed the predicted MF density profiles when the chemical potential μ for MF is optimized so as to be in the best agreement possible with the corresponding MC simulation. For the situation of two hard walls all predictions (except the standard MF ones) seem to be in good agreement with MC data, with the μ-optimized MF the best by a slight margin. For the other external potential, the new ML Ansatz of Eq.(4.2) performs somewhat better than μ-optimized MF prediction, because the density oscillations are more accurately modelled.

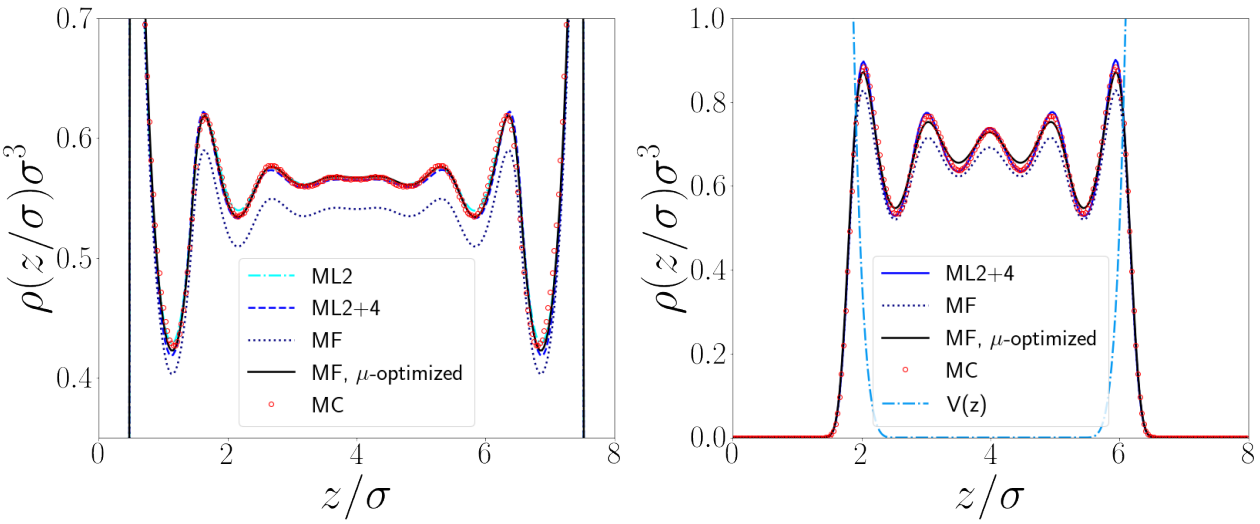

(a) The case of two planar hard walls at $\mu^* = 0$ ($\rho_{bulk} = 0.57$).

(b) The case of the external potential $V(z)$ (light blue dot-dashed line) at $\mu^* = 1.25$. The $V(z)$ used has parameters $a = 6.0, b = 0.18, c = 4.5$.

Figure 4.7: The predicted density profiles of the ML Ansatz Eq.(4.2). The purple dotted line is the prediction of MF and the black solid line the prediction of MF when the chemical potential μ is tweaked so that the result is in the best possible agreement with the MC simulation.

To investigate whether the ML functional of Eq.(4.2) performs overall better than μ-optimized MF, we generated 108 MC density profiles for varying out-of-sample external potentials $V(z)$ and chemical potentials $\mu^* \in (-1.25, 1.25)$ not in the original training set. (In the same way as the original training set was generated.) We compared the predicted densities of the ML functional Eq.(4.2) and μ-optimized MF for these $V(z)$ and μ, by computing the total squared errors J with respect to MC as in Eq.(3.1). In terms of J, ML performs 14% better than a μ-optimized MF, so it predicts the shape of the densities better than MF. This can be concluded because μ-optimized MF almost surely predicts the bulk density perfectly.

4.3 The temperature dependence of the ML functional

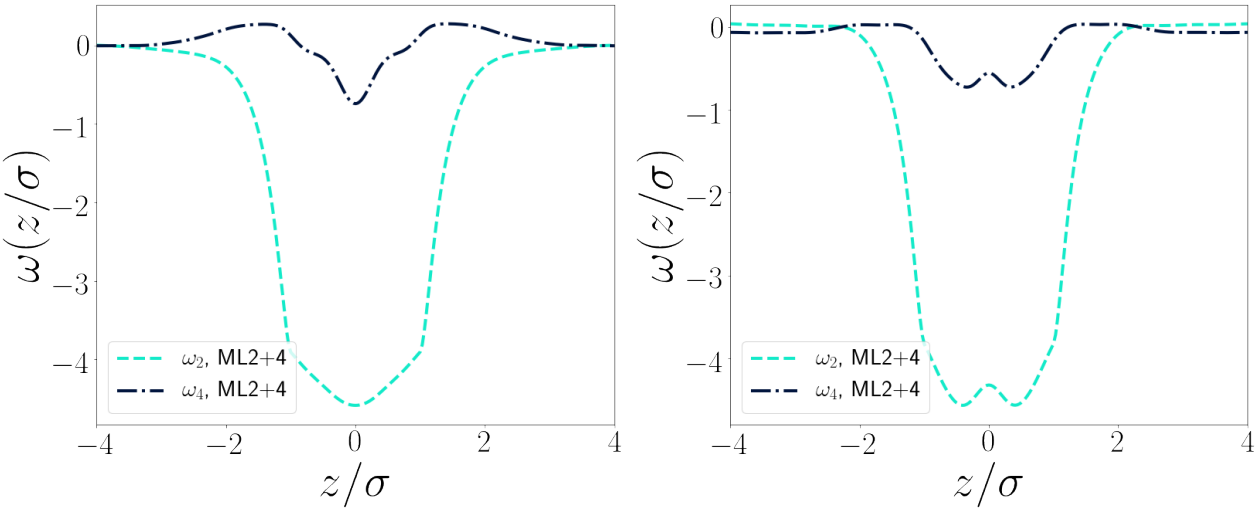

(a) For $T^* = 1.6$. (b) For $T^* = 3.0$.

Figure 4.8: The trained $\omega_2(z)$ and $\omega_4(z)$ of Eq.(4.2) for $T^* = 1.6$ and $T^* = 3.0$.

So far we only considered $\epsilon^* = 0.5$, or equivalently, the reduced temperature $T^* = 1/\epsilon^* = 2.0$. To investigate the temperature dependence of the ML kernels of Eq.(4.2), we generated the same MC data sets as used in the case $T^* = 2.0$ for different temperatures $T^* \in \{1.6, 1.8, 2.0, 2.2, 2.6, 3.0\}$, and trained the functional Eq.(4.2) for each of those temperatures. The resulting kernels for $T^* = 1.6$ and $T^* = 3.0$ are shown in Figure 4.8. In Figure 4.9 we plotted all the resulting $\omega_2(z)$ and $\omega_4(z)$ of Eq.(4.2) in the same figures for comparison.

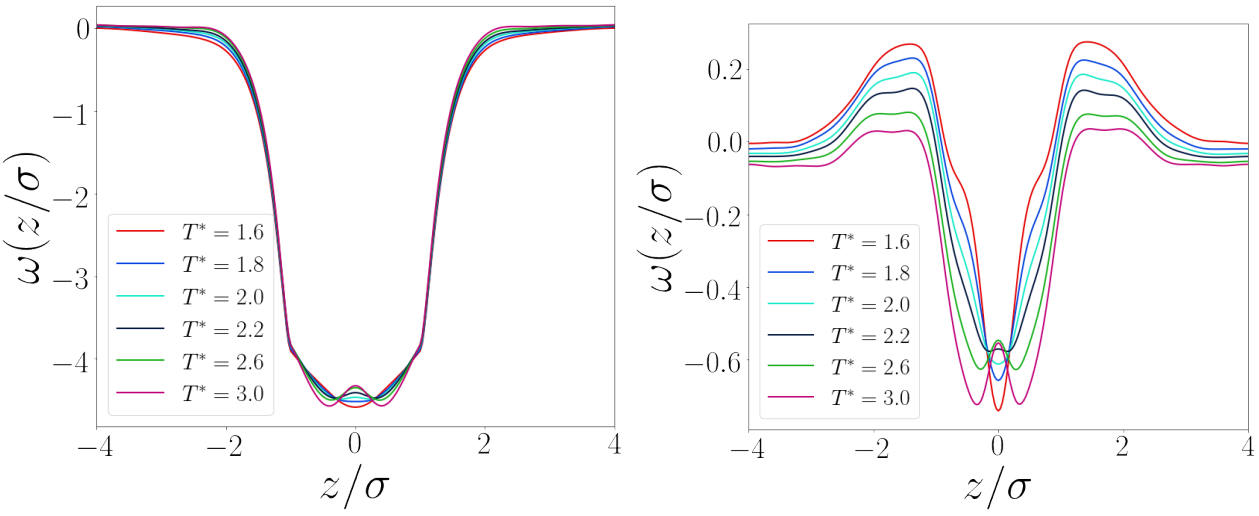

(a) The trained $\omega_2(z)$ kernels. (b) The trained $\omega_4(z)$ kernels.

Figure 4.9: The ML-trained weighting kernels of Eq.(4.2) for different temperatures $T^* \in \{1.6, 1.8, 2.0, 2.2, 2.6, 3.0\}$ plotted for comparison in a single figure.

From Figure 4.8 and Figure 4.9 it is clear that the exact shape of the ML-trained weighting kernels are temperature-dependent and do not scale precisely in a linear fashion with T^*, that is, they do not scale linearly with either the Lennard-Jones attraction parameter ϵ or the temperature k_BT. However, the general form of all the $\omega_2(z)$ and all the $\omega_4(z)$ kernels are the same and are of the same order of magnitude. At low temperatures, the minimum of both $\omega_2(z)$ and $\omega_4(z)$ is at $z = 0$, while at higher temperatures there are two minima equidistantly located from $z = 0$. Also the $\omega_4(z)$ kernels seem to increase linearly with T^* in the range $|z/\sigma| > 1$. It is unclear why the temperature dependence of the weighting kernels has these features.

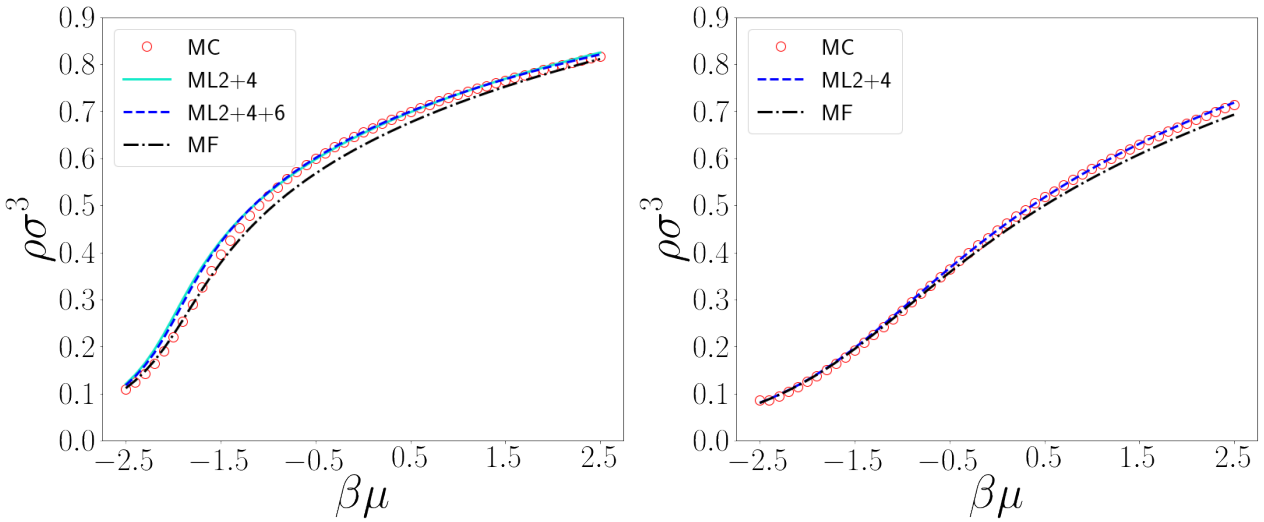

(a) At $T^* = 1.6$. (b) At $T^* = 3.0$.

Figure 4.10: The equation of state for $\rho_{bulk}(\mu)$ at two different temperatures T^*.

We also compared the performance of ML for these different values of T^* and it turns out that ML with Ansatz Eq.(4.2) performs significantly better at high T^* than at low T^*. In Figure 4.10 we show the equation of state for $T^* = 1.6$ and $T^* = 3.0$. From Figure 4.10 it is clear that at $T^* = 3.0$ ML performs well also at low to medium μ in contrast with the case $T^* = 1.6$. Overall the performance is better than MF. Because the performance of ML with Ansatz Eq.(4.2) at $T^* = 1.6$ is not so good at low to medium μ, we tried Eq.(4.2) with an added extra term of sixth order in the densities, $\frac{\epsilon}{2}\int\int dzdz'\rho^3(z)\rho^3(z')\omega_6(|z-z'|)$, the result is shown in Figure 4.10a. The new Ansatz yields slightly better results but still fails to accurately reproduce the MC densities at low to medium μ. An extra term of third order in the density, $\frac{\epsilon}{2}\int\int dzdz'\rho(z)\rho(z')(\rho(z)+\rho(z'))\omega_3(|z-z'|)$, surprisingly did not seem to improve the results at all.

4.4 The direct correlation function

When an Ansatz for the functional is trained, the 2-body direct correlation function can be computed from[9]

$$c^{(2)}(\mathbf{r},\mathbf{r}') = -\beta \frac{\delta^2 \mathcal{F}_{exc}^{LJ,ML}[\rho(\mathbf{r})]}{\delta\rho(\mathbf{r})\delta\rho(\mathbf{r}')}. \tag{4.3}$$

However, the functionals we used are trained in planar geometries, so they only depend on a single variable z and the functional derivatives in Eq.(4.3) with respect to $\rho(\mathbf{r})$ are not defined. Assuming that the attractive part of the unknown functional $\mathcal{F}_{exc}^{LJ,ML}[\rho(\mathbf{r})]$, that is, the functional of the density profile $\rho(\mathbf{r})$ in $3D$, is of the same general form as Eq.(4.1) or Eq.(4.2), and that the corresponding unknown weighting kernels $\Omega_i(\mathbf{r})$ are spherically symmetric, so that $\Omega_i(\mathbf{r}) = \Omega_i(r)$ with r the radial coordinate in the spherical coordinate system, the relation between the trained $\omega_i(z)$ and the $\Omega_i(r)$ by definition is

$$\omega_i(z) = 2\pi \int_0^\infty s\ ds\ \Omega_i(\sqrt{s^2+z^2}), \tag{4.4}$$

where s denotes the radial coordinate in the cylindrical coordinate system. It is possible, as is shown in Appendix A.2, to cast Eq.(4.4) to an explicit form for $\Omega_i(r)$. The result is

$$\Omega_i(r) = \left(\frac{-1}{2\pi z} \frac{d\omega_i(z)}{dz} \right)\Bigg|_{z=r}. \tag{4.5}$$

The attractive part of $\mathcal{F}_{exc}^{LJ,ML}[\rho(\mathbf{r})]$ for ML with Ansatz Eq.(4.2) is then

$$\mathcal{F}_{exc,att}^{LJ,ML}[\rho(\mathbf{r})] = \frac{\epsilon}{2}\int\int d\mathbf{r}d\mathbf{r}'\rho(\mathbf{r})\rho(\mathbf{r}')\Omega_2(|\mathbf{r}-\mathbf{r}'|) + \frac{\epsilon}{2}\int\int d\mathbf{r}d\mathbf{r}'\rho^2(\mathbf{r})\rho^2(\mathbf{r}')\Omega_4(|\mathbf{r}-\mathbf{r}'|). \tag{4.6}$$

In bulk, $\rho(\mathbf{r}) = \rho$ and the 2-body direct correlation function Eq.(4.3) for the attractive part of the functional reduces to

$$c_{att}^{(2),LJ,ML}(\mathbf{r},\mathbf{r}') = c_{att}^{(2),LJ,ML}(r) = -\epsilon^*\Omega_2(r) - 6\epsilon^*\rho^2\Omega_4(r). \tag{4.7}$$

The repulsive part of $c^{(2),LJ}(r)$ can be modelled with the exact solution $c_{rep}^{(2),PY}(r)$ to the Ornstein-Zernike equation (using the Percus-Yevick closure) of hard spheres with (effective) diameter d given in Eq.(2.32). The complete expression for $c_{rep}^{(2),PY}(r)$ is given in [9]. The 2-body direct correlation function in bulk fluid at density ρ is then

$$\begin{aligned} c^{(2),LJ}(r) &= c_{rep}^{(2),PY}(r) + c_{att}^{(2),LJ,ML}(r) \\ &= c_{rep}^{(2),PY}(r) - \epsilon^*\Omega_2(r) - 6\epsilon^*\rho^2\Omega_4(r). \end{aligned} \tag{4.8}$$

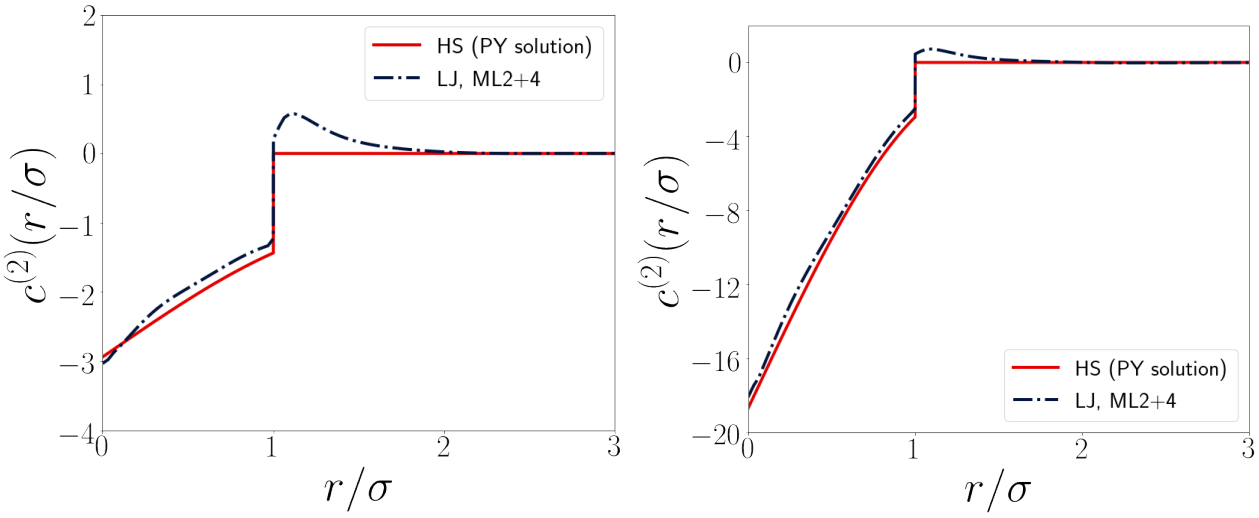

(a) At bulk density $\rho = 0.3$.

(b) At bulk density $\rho = 0.8$.

Figure 4.11: The 2-body direct correlation function in bulk at temperature $T^* = 2.0$ as generated by ML from Eq.(4.8) and the Percus-Yevick exact solution for hard spheres with effective diameter d given in Eq.(2.32).

In Figure 4.11 the 2-body direct correlation function in bulk as generated by ML from Eq.(4.8) is plotted at $T^* = 2.0$ for bulk densities $\rho = 0.3$ and $\rho = 0.8$. The Percus-Yevick solution is also shown.

When $c^{(2),LJ}(r)$ is computed, it is possible (but we omit this due to time constraints) to compute the structure factor $S(q)$ from the Fourier transform $\hat{c}(q)$ of $c^{(2),LJ}(r)$, by the relation[10]

$$S(q) = \frac{1}{1 - \rho\hat{c}(q)}. \tag{4.9}$$

5 Summary, discussion of the results and conclusion

We used Machine Learning to approximate the excess Helmholtz free-energy functional $\mathcal{F}^{LJ}_{exc}[\rho(z)]$ of a supercritical Lennard-Jones fluid in planar geometries in 3 dimensions. $\mathcal{F}^{LJ}_{exc}[\rho(z)]$ was split into two parts, a repulsive and an attractive part. The repulsive part was modelled by hard spheres with an effective diameter d given by Eq.(2.32), for which we used the Rosenfeld functional Eq.(2.21). The attractive part was to be determined by ML, for which we took the MF functional Eq.(2.35) as a starting point in the training process.

As training data, we used 225 MC-simulated density profiles $\rho_i^{MC}(z)$ corresponding to a pre-defined set of external potentials $V_i(z)$ and chemical potentials μ_i, at fixed temperature k_BT/ϵ. After making an Ansatz for $\mathcal{F}^{att}[\rho(z)]$ in terms of one or more weighting kernels $\omega_k(z)$ that were to be determined by ML, the functional was 'trained' by minimizing the discrepancy of the $\rho_i^{ML}(z)$ it generates for each $(\mu, V(z))_i$ in the training set with the associated MC density $\rho_i^{MC}(z)$. In practice this meant numerically constructing the $\omega_k(z)$ in such a way that the criterion J of Eq.(3.1) over the training set, that is, the difference between the ML-predicted density profiles and the MC densities, was minimized. The minimization criterion was based on the practical grounds of numerical efficiency and calculational convenience, and was not chosen for physical or statistical reasons.

Different Ansatzes for $\mathcal{F}^{att}[\rho(z)]$ were trained, and the resulting trained functionals were tested on performance by making density predictions in out-of-sample situations, such as the case of confinement between two planar hard walls and in certain external potentials not in the training set. These predictions were compared to MC simulations and the performance increase with respect to MF was computed. Furthermore, we used the trained functionals to predict the equation of state $\rho_{bulk}(\mu)$ and $P(\rho)$ and compared the results to those of MF and to MC simulations. Finally the temperature dependence of the functionals was explored by repeating the training process for different values of ϵ^*.

As we pointed out in the introduction, it is important for theoretical understanding to physically interpret the resulting ML-trained functionals, although this is very difficult because there is no theoretical basis for an Ansatz such as Eq.(4.2), and we simply tried to restrict as much as possible the number of weighting kernels used and the mathematical complexity of the Ansatz. Only the mean-field like kernel in Eq.(4.1) can be loosely interpreted as an empirically-determined effective Lennard-Jones interaction energy after integration over two dimensions. Evidently the most challenging aspect of using ML for constructing functionals is designing a good Ansatz for the mathematical form of the functional. This Ansatz should preferably be based on DFT grounds in order to be able to meaningfully interpret the results after training and improve theoretical understanding. It should also not include too many unknown parameters or weighting kernels in order to prevent overfitting. We successfully restricted the number of weighting kernels used, and still trained functionals that generated fairly accurate predictions that are overall better than those of MF. However, we failed to base our Ansatzes on a true theoretical basis, and are therefore limited in our ability to extract new theoretical insight from the ML-trained functionals that has a direct impact on contemporary classical DFT.

ML applied to a simple Ansatz like Eq.(4.1) appears to be overall superior to MF in terms of predicting the shape of density profiles for varying external potentials and for confinement between hard walls. The predicted densities are more oscillatory than those of MF, which is in better agreement with the MC simulations. The Ansatz Eq.(4.2) for $\mathcal{F}^{att}[\rho(z)]$ performs significantly better than the mean-field like Ansatz Eq.(4.1), but extra terms including terms of third and sixth order in the density do not seem to meaningfully improve the results any further. ML with Ansatz Eq.(4.2) is slightly more accurate, in terms of the squared residuals as in Eq.(3.1), than 'μ-optimized' MF, that is, mean field theory with the chemical potential tweaked so as to minimize the difference with MC in the sense of Eq.(3.1). The ML-predicted equation of state is overall better than that of MF, but lacks accuracy for low to medium densities slightly above the ideal-gas regime, where the predictions of MF are better. The predicted density and pressure for medium to high μ are in good agreement with MC simulations. We expect that the discrepancy in predictions for low to medium μ are due to the definition of the minimization criterion J in Eq.(3.1). The functional learns by minimizing the squared differences with respect to MC over the entire data set and over the entire system length, without paying special attention to the predicted bulk density, or equivalently, to the equation of state. Therefore an incorrectly predicted density 'peak' will have a more severe impact on the next iteration's weighting kernels, compared to an incorrectly predicted bulk density associated with a smaller 'cost' in terms of the criterion J. Furthermore, the results did not seem to improve when using a larger MC data set of about twice the number of density profiles. This is most likely because the entire range of interesting values for μ is already included in the original data set.

The shape of the weighting kernels in Eq.(4.2) are temperature dependent and do not precisely scale linearly with the temperature, in contrast to what might be expected on basis of mean field theory as in Eq.(2.34)). Because the entire MC-dataset has to be separately simulated for each value of ϵ^*, due to time constraints we were unable to train the functional for a sufficient number of values for ϵ^* to draw quantitative conclusions about the temperature dependence of $\mathcal{F}^{att}[\rho(z)]$. We can however conclude that the performance of the ML-trained functionals for high temperatures is significantly better than the performance at low temperatures, especially at those close to the critical point. This is also what Lin. et al. found in the $1D$ case[8]. For high temperatures, the equation of state for the bulk density is predicted accurately even for low to medium μ. We expect that the physics close to the critical point is more difficult to model with a very simple Ansatz like Eq.(4.2), and that a more sophisticated Ansatz based on DFT grounds is required.

References

[1] Plischke, M. and Bergersen, B., *Equilibrium Statistical Physics*, 3rd edition, Singapore: World Scientific, 2007.

[2] Jeanmairet, G., Levy, N., Levesque, M. and Borgis, D., *Introduction to Classical Density Functional Theory by a Computational Experiment*, J. Chem. Educ. 2014, 91, 12, 2112-2115, arXiv:1401.1679v3, DOI: 10.1021/ed500049m.

[3] Roth., R., *Introduction to Density Functional Theory of Classical Systems: Theory and Applications*, lecture notes, ITAP, Universität Stuttgart and Max-Planck-Institut für Metallforschung, Stuttgart, November 2006.

[4] Peng, B. and Yu, Y., *A Density Functional Theory with a Mean-field Weight Function: Applications to Surface Tension, Adsorption, and Phase Transition of a Lennard-Jones Fluid in a Slit-like Pore*, J. Phys. Chem. B, 2008, 112 (48), 15407-15416, DOI: 10.1021/jp805697p.

[5] Choudhury, N. and Ghosh, S., *New Weighted Density Functional Theory Based on Perturbative Approach*, J. Phys. Chem. B, 2003, 107, 7155-7161, DOI: 10.1021/jp0270553.

[6] Hastie, T., Tibshirani, R. and Friedman, J., *The Elements of Statistical Learning*, second edition, Springer Series in Statistics, Springer New York Inc., New York, NY, USA, (2009).

[7] Brockherde, F., Vogt, L., Li. L., Tuckerman, M., Burke, K. and Müller, K., *Bypassing the Kohn-Sham equations with machine learning*, Nature Communications 8, Article number: 872 (2017), DOI: 10.1038/s41467-017-00839-3.

[8] Lin, S.C., et al., *A classical density functional from machine learning and a convolutional neural network* , SciPost Phys. 6, 025 (2019), arXiv:1811.05728v3, DOI: 10.21468/SciPostPhys.6.2.025.

[9] Van Roij, R., *Soft Condensed Matter Theory*, lecture notes, Soft condensed matter theory NS-TP453M, Utrecht University, February 2018.

[10] Dijkstra, M., *Modelling and Simulation*, lecture notes, Modelling and simulation NS-TP432M, Utrecht University, 2018.

[11] Yu, Y., *A novel weighted density functional theory for adsorption, fluid-solid interfacial tension, and disjoining properties of simple liquid films on planar solid surfaces*, J. Chem. Phys. 131, 024704 (2009), DOI: 10.1063/1.3174928.

[12] Hayashi, F., *Econometrics*, Princeton University Press, 2000.

[13] Loscar, E.S. et al., *Spinodals and critical point using short-time dynamics for a simple model of liquid*, J. Chem. Phys. 144, 134501 (2016), DOI: 10.1063/1.4944926.

A Appendix

A.1 The xy-integrated attractive Lennard-Jones potential

We wish the evaluate

$$U_{att,z}(z) = \int_{-\infty}^{\infty}\int_{-\infty}^{\infty} \frac{U_{att}(\sqrt{x^2+y^2+z^2})}{\epsilon} dxdy, \tag{A.1}$$

where $U_{att,z}(r)$ is the attractive part of the Lennard-Jones potential given in Eq.(2.31) and $r = \sqrt{x^2+y^2+z^2}$, the spherical radial coordinate. It is convenient to do this integral in cylindrical coordinates (s, ϕ, z), so that it becomes

$$U_{att,z}(z) = 2\pi \int_0^{\infty} s\ ds\ \frac{U_{att}(\sqrt{s^2+z^2})}{\epsilon}. \tag{A.2}$$

Now notice that if $z/\sigma > 1$, also $r/\sigma > 1$ and therefore $U_{att}(r) = U(r)$. And if $z/\sigma \leq 1$, $U_{att}(r) = 0$ for $s^2 \leq \sigma^2 - z^2$, and $U_{att}(r) = U(r)$ otherwise. Therefore, by substituting the expression for Eq.(2.29), we have

$$U_{att,z}(z) = \begin{cases} 8\pi \displaystyle\int_{\sqrt{\sigma^2-z^2}}^{\infty} s\ ds \left(\left(\frac{\sigma^2}{s^2+z^2}\right)^6 - \left(\frac{\sigma^2}{s^2+z^2}\right)^3\right), & \text{if } |z| \leq \sigma. \\ 8\pi \displaystyle\int_0^{\infty} s\ ds \left(\left(\frac{\sigma^2}{s^2+z^2}\right)^6 - \left(\frac{\sigma^2}{s^2+z^2}\right)^3\right), & \text{if } |z| > \sigma. \end{cases} \tag{A.3}$$

These two elementary integrals can be computed analytically. Consider the indefinite integral

$$I = 8\pi \int s\ ds \left(\left(\frac{\sigma^2}{s^2+z^2}\right)^6 - \left(\frac{\sigma^2}{s^2+z^2}\right)^3\right). \tag{A.4}$$

Now make the substitution $u = s^2 + z^2$, so that $du = 2s\ ds$, and therefore

$$\begin{aligned} I &= 4\pi \int du \left(\left(\frac{\sigma^2}{u}\right)^6 - \left(\frac{\sigma^2}{u}\right)^3\right) \\ &= \frac{-4\pi\sigma^{12}}{5u^5} + \frac{4\pi\sigma^6}{2u^2} \\ &= \frac{-4\pi\sigma^{12}}{5(s^2+z^2)^5} + \frac{4\pi\sigma^6}{2(s^2+z^2)^2}. \end{aligned} \tag{A.5}$$

Evaluating Eq.(A.5) on the integration limits of the two definite integrals in Eq.(A.3) yields the result

$$U_{att,z}(z) = \begin{cases} -\dfrac{6\pi\sigma^2}{5}, & \text{if } |z| \leq \sigma. \\ \dfrac{2\pi\sigma^6(2\sigma^6 - 5z^6)}{5z^{10}}, & \text{if } |z| > \sigma. \end{cases} \tag{A.6}$$

A.2 The relation between the general weighting kernels and the projected, ML-trained kernels

Given the relation

$$\omega_i(z) = 2\pi \int_0^\infty s\ ds\ \Omega_i(\sqrt{s^2+z^2}), \tag{A.7}$$

where $\omega_i(z)$ is known, we wish to derive an explicit expression for $\Omega_i(r)$. First we make the substitution $u^2 = s^2 + z^2$, so that $s = \sqrt{u^2 - z^2}$ and $ds = u\ du/s$. The new integration domain is $[z, \infty)$. Eq.(A.7) then reduces to

$$\omega_i(z) = 2\pi \int_z^\infty u\ du\ \Omega_i(u). \tag{A.8}$$

We can differentiate both sides to z and use the Leibniz integral rule. The u in the integrand has become a 'dummy' integration variable, so the partial derivative of it with respect to z is zero. Therefore the only term is due to the lower integration limit. The result is

$$\frac{d\omega_i(z)}{dz} = -2\pi z \Omega_i(z). \tag{A.9}$$

We can rewrite this as an explicit expression for $\Omega_i(r)$:

$$\Omega_i(r) = \left(\frac{-1}{2\pi z} \frac{d\omega_i(z)}{dz} \right) \Bigg|_{z=r}, \tag{A.10}$$

where we replaced the variable z with r, purely for cosmetic reasons, to emphasize that the weighting kernels $\Omega_i(r)$ are assumed to be spherically symmetric and therefore only dependent on the spherical radial coordinate r.

A.3 A brief note regarding computational requirements

To simulate the MC density profiles we used for the training data set, we used the C programming language and followed guidelines in [10] to write an MC simulation code for the truncated Lennard-Jones potential. We implemented a so-called 'cell list' method where the system is divided into cubic cells of length equal to the truncation distance 2.5σ, and particles only interact with particles in neighbouring cells (including those due to periodic boundary conditions). This significantly reduced computational complexity versus a naive implementation where for each particle a loop over all the other particles in the system is initiated. An MC-simulated density profile in our training set took somewhere between 20 and 50 hours to generate on a regular processing unit, depending on the chemical potential μ and hence the bulk density. This long time was required to simulate with an accuracy great enough to be used for training purposes, due to the large number of 32 grid points per particle. Because we simulated 225 density profiles for 6 different temperatures, that is, 1350 in total, the total computing time necessary would be about 3 to 4 years on a single computer. Thus we had to resort to using a large computer cluster where we ran an entire training set of 225 density profiles on 225 computers at once. We also used C to simulate all the equations of state and the out-of-sample density profiles, which required comparable computational effort.

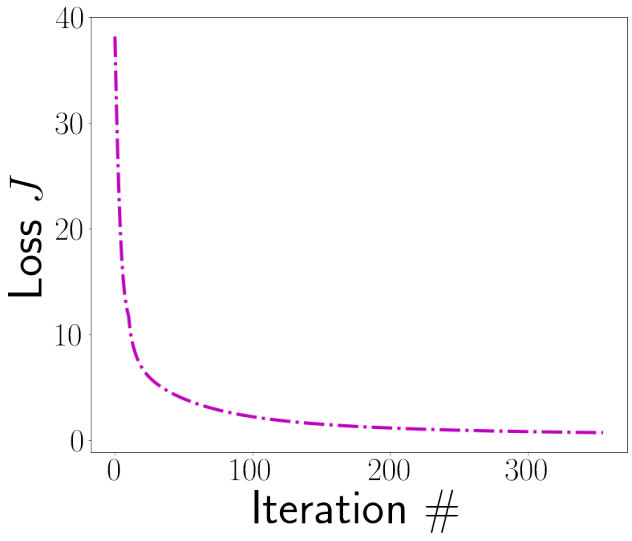

Figure A.1: The loss J as defined in Eq.(3.1) versus the iteration number, for training of Ansatz Eq.(4.2) at temperature $T^* = 2.0$.

The training process was written in Python 3, in the Jupyter Notebook environment to be specific. The authors of [8] were so kind as to share the implementation of the $1D$ training process they used with us, so we were able to use their implementation as a starting point, although many changes were made due to the different Ansatzes we postulated and the different dynamics in $3D$. In contrast to the MC simulations, the training process itself took much shorter than we initially expected. For any Ansatz for $\mathcal{F}^{att}[\rho(z)]$ we postulated it was not more than a few hours, three at most, on a single computer. In Figure A.1 the loss J as defined in Eq.(3.1), for training of Ansatz Eq.(4.2) at temperature $T^* = 2.0$, is plotted versus the iteration number of the training process. It can be seen that especially the first few iterations rapidly improve the performance of ML. Generating a density profile with ML by iteratively solving the Euler-Lagrange equation with the Picard iteration method, took in order of a few seconds, no more than ten. Generating the equation of state with ML took a few minutes. This is without doubt a large advantage of using ML compared to using MC simulations.